Computers and Fluids 133 (2016) 151–169

Contents lists available at ScienceDirect

Computers and Fluids

journal homepage: www.elsevier.com/locate/compfluid

Numerical aspects of Eulerian gas–particles flow formulations

Cesar M. Venier[a,*], Santiago Marquez Damian[a,c], Norberto M. Nigro[a,b]

[a] Research Center for Computational Methods (CIMEC), CONICET, Santa Fe, Argentina
[b] Facultad de Ingenieria y Ciencias Hidricas, Universidad Nacional del Litoral, Santa Fe, Argentina
[c] Facultad Regional Santa Fe, Universidad Tecnologica Nacional, Santa Fe, Argentina

ARTICLE INFO

Article history:
Received 27 October 2015
Revised 10 March 2016
Accepted 4 May 2016
Available online 7 May 2016

Keywords:
Conservative method
Two-fluid model
Granular flow
OpenFOAM
Fluidized bed

ABSTRACT

An Eulerian two-fluid numerical solver with kinetic-frictional theory for granular flows has been implemented and validated on the open-source code platform OpenFOAM®. Several aspects of the numerical treatment are discussed: maximum packing and phase disappearing limits, phase accumulation, cell-face fields interpolation and reconstruction practices, drag coupling approaches and different levels of conservativeness of the momentum equations. These last two topics are studied in depth. On the drag coupling analysis, it is observed that the *partially implicit method* (PIM) exhibits a convergence performance similar to the *partial elimination algorithm* (PEA) for a Geldart B particulate fluidized bed problem. But, for strongly coupled conditions (e.g. smaller particles) the use of the PEA becomes essential to meet a prescribed convergence criteria. Secondly, the conservativeness of the advective term of the momentum equations is analyzed by comparing three formulations of the advective term (the *conservative form*, the *nonconservative form* and the *phase-intensive form*). The impact of each formulation on the velocity field prediction is quantified for a shallow water problem and then extended to two-dimensional gas–liquid and gas–particle systems. The results show that the adoption of a conservative formulation is crucial to obtain accurate solutions in transient problems. However, for time-averaged analysis, which is often used for the study of fluidized bed systems, the nonconservative *phase-intensive form* is still a useful tool.

1. Introduction

In the last decades, the CFD modeling became a strong tool to study fluidized bed systems and to complement the experimental measures [1–10]. Among the available numerical techniques, the Eulerian two-fluid model [11,12] with kinetic-frictional theory of granular flow closure provides a low-cost approach for the simulation and design of large-scale gas–particles systems.

Investigations on particulate flows gained attention since the development of the kinetic theory of granular flow [13–15] derived from the general theory of non-uniform dense gases of Chapman and Cowling [16]. In this approach, the granular phase is formed by uniform solid spheres and only binary instantaneous collisions are considered. Early granular flow simulations relied on constant solid viscosity and simple elasticity-type correlations to account for the solid phase normal stresses [17,18]. In the kinetic theory of granular flow, the effects of the particles interactions on the phase rheology are modeled by means of the granular temperature, which is related to the random motion of the particles. This approach has the advantage of having a deeper phenomenological basis than the early theories and several comparisons may be found in the literature [9,10]. Further on, it became clear that the hypothesis of instantaneous collisions of the kinetic theory no longer endure for high particle concentration. In these conditions, where rubbing and friction between particles may occur, the solid phase rheology is often modeled by the frictional theory [19–21]. The mathematical closure of the problem is obtained by the coupling between phases through the interphase forces. Usually, for fluidized bed simulations, the lift and virtual mass effects are neglected and only the drag force term is considered. Many correlations for the drag coefficient are available [15,22–27] and their performance in fluidized bed problems has been investigated over the years [3,26,28].

The Eulerian gas–particle flow model consists of treating both phases as interpenetrating continua which leads to a system of averaged Navier–Stokes equations [12]. These equations are solved along with the granular energy balance equation based on the kinetic-frictional theory of granular flow and the mass conservation equations of each phase. There are many factors that compromise the stable behavior of the numerical algorithm devised to

* Corresponding author.
E-mail addresses: cesarvenier@gmail.com (C.M. Venier), santiagomarquezd@gmail.com (S. Marquez Damian), norberto.nigro@cimec.santafe-conicet.gov.ar (N.M. Nigro).

http://dx.doi.org/10.1016/j.compfluid.2016.05.003
0045-7930/

solve this system of equations. In particular, the coupling algorithm through the drag force and the different levels of conservativeness of the advective term formulation are still topics of discussion nowadays.

The condition at which the solid phase tends to disappear leads to a singular momentum equation. This translates into highly oscillatory solutions of the phase velocity field, which can be managed in several ways. Oliveira et al. [29] proposed a nonconservative reformulation of the phase momentum equations, usually referred as the *phase-intensive form* [30,31]. A consequence of this treatment is the appearance of a singularity in the solid stress tensor term when the solid volume fraction tends to zero, which can be easily avoided through numerical manipulation. This improvement has the cost of leaving behind the conservative form of the momentum equations. Nonconservative formulations could lead to inaccurate predictions of the velocity field when shock waves are present [32,33], however, due to the inclusion of the phase volume fraction field α_i in the momentum equations, there is more than one nonconservative formulation possible to be considered (namely the fully *nonconservative form* and the *phase-intensive form*). It is a purpose of the present work to bring some insight into the impact of the different advective term formulations in commonly studied gas–particle problems through a comparative analysis.

The coupling between phases given by the drag force term may be handled in several ways to reach a converged solution in a reasonable time. One way is to adopt the *partially implicit method* (PIM), which is based on splitting the drag term of the *i*-phase momentum equation and treating the *i*-phase velocity contribution as an unknown. The computational implementation of this method is of low complexity and it is currently adopted in many multiphase flow solvers [34]. But, as it is shown by Oliveira et al. [35], the convergence of the iterative procedure for drag dominated problems could be compromised. Another approach is the *partial elimination algorithm* (PEA) based on the work of Spalding [36]. This method allows a partial decouple of each phase momentum equation which, under certain conditions, has a significant impact on the solution convergence. This feature has been investigated in the literature [35,37,38] and the method has been adopted by several authors [31,39].

In this work, a conservative gas–particle flow solver with kinetic-frictional theory closure has been developed and implemented on the open source code OpenFOAM® [34]. The solver modules are based on the finite volume method and the PIMPLE algorithm [40,41] has been used for the pressure–velocity coupling. Several aspects of the numerical treatment are investigated to recognize common pathologies of gas–particles flow problems and to determine some general criteria to avoid them. On the advective term formulations, three levels of conservativeness are considered and tested on standard multiphase problems. For the phases coupling, the PEA has been implemented and its convergence performance is compared against the PIM. The volume fraction bounding has been achieved by means of the MULES integrator [42,43] based on a multidimensional flux corrected transport scheme [44] and the packing limit condition has been fulfilled with an implicit treatment of the particle pressure contribution to the flux, given by the kinetic-frictional theory models.

As a summary of the present work, the sections are organized as follows. In Section 2, the governing equations and closure theories are presented. Section 3 describes the numerical procedure and the general algorithm. In Section 4, two gas–particles cases are simulated and the numerical performance of the solver is tested. Finally, in Section 5, a sensitivity analysis of the different levels of conservativeness of the advective term is performed through a one-dimensional study and then extended to a series of two-dimensional multiphase test cases.

2. Multiphase model

2.1. Governing equations

In this work, an Eulerian gas–particle flow system is considered, in which both phases are treated as an interpenetrating continua and the volumetric phase fractions verify that $\alpha_s + \alpha_g = 1$. Here, the subscript s represents the solid phase and the subscript g represents the gas phase. The continuity and momentum equations for the solid phase are:

$$\frac{\partial}{\partial t}(\rho_s\alpha_s) + \nabla\cdot(\rho_s\alpha_s\mathbf{u}_s) = 0 \tag{1}$$

$$\frac{\partial}{\partial t}(\rho_s\alpha_s\mathbf{u}_s) + \nabla\cdot(\rho_s\alpha_s\mathbf{u}_s\mathbf{u}_s) = -\alpha_s\nabla p - \nabla p_s + \nabla\cdot(\alpha_s\boldsymbol{\tau}_s) + \rho_s\alpha_s\mathbf{g} + K_{sg}(\mathbf{u}_g - \mathbf{u}_s) \tag{2}$$

while for the gas phase, the equations are:

$$\frac{\partial}{\partial t}(\rho_g\alpha_g) + \nabla\cdot(\rho_g\alpha_g\mathbf{u}_g) = 0 \tag{3}$$

$$\frac{\partial}{\partial t}(\rho_g\alpha_g\mathbf{u}_g) + \nabla\cdot(\rho_g\alpha_g\mathbf{u}_g\mathbf{u}_g) = -\alpha_g\nabla p + \nabla\cdot(\alpha_g\boldsymbol{\tau}_g) + \rho_g\alpha_g\mathbf{g} + K_{sg}(\mathbf{u}_s - \mathbf{u}_g) \tag{4}$$

where the shear stress tensors are modeled as:

$$\boldsymbol{\tau}_s = \mu_s\left[\nabla\mathbf{u}_s + \nabla\mathbf{u}_s^T\right] + \left(\lambda_s - \frac{2}{3}\mu_s\right)(\nabla\cdot\mathbf{u}_s)\mathbf{I} \tag{5}$$

$$\boldsymbol{\tau}_g = \mu_g\left[\nabla\mathbf{u}_g + \nabla\mathbf{u}_g^T\right] - \frac{2}{3}\mu_g(\nabla\cdot\mathbf{u}_g)\mathbf{I} \tag{6}$$

Here ρ_i is the phase density field, $\mathbf{u}_i$ the phase velocity field, p the shared pressure field, p_s the particle pressure field, $\mathbf{g}$ the gravitational acceleration, K_{sg} the global drag coefficient, μ_i the phase dynamic viscosity and λ_i the phase bulk viscosity.

The lift and virtual mass effects are neglected and the phases are coupled through the drag force term. Different drag coefficient correlations have been developed over the years, but only the models used in this work are presented. The drag coefficient given by the Wen–Yu model [23] is:

$$K_{sg} = 0.75\frac{C_d\alpha_s\alpha_g^{-1.65}\rho_g|\mathbf{u}_g - \mathbf{u}_s|}{d_p} \tag{7}$$

here d_p is the particle diameter, C_d is the drag form coefficient defined as:

$$C_d = \begin{cases} \dfrac{24}{Re_p}(1 + 0.15Re_p^{0.687}), & Re_p < 1000 \\ 0.44 & Re_p \geq 1000 \end{cases} \tag{8}$$

where

$$Re_p = \frac{\rho_g d_p|\mathbf{u}_g - \mathbf{u}_s|}{\mu_g} \tag{9}$$

Also, the drag coefficient for the Gidaspow model [15] is:

$$K_{sg} = \begin{cases} 150\dfrac{\mu_g\alpha_s^2}{d_p^2\alpha_g^2} + 1.75\dfrac{\rho_g\alpha_s}{d_p\alpha_g}|\mathbf{u}_g - \mathbf{u}_s|, & \alpha_s > 0.2 \\ 0.75\dfrac{C_d\alpha_s\alpha_g^{-1.65}\rho_g|\mathbf{u}_g - \mathbf{u}_s|}{d_p} & \alpha_s < 0.2 \end{cases} \tag{10}$$

and the drag coefficient for the Syamlal–O'Brien model [24] is:

$$K_{sg} = 0.75\frac{C_e\alpha_s\alpha_g\rho_g|\mathbf{u}_g - \mathbf{u}_s|}{d_p v_{rs}^2} \tag{11}$$

where

$$v_{rs} = 0.5\left[A - 0.06Re_p + \sqrt{(0.06Re_p)^2 + 0.12Re_p(2B - A) + A^2}\right] \tag{12}$$

$$A = \alpha_g^{4.14}, \quad B = \begin{cases} 0.8\alpha_g^{1.28} & , \alpha_g \leq 0.85 \\ \alpha_g^{2.65} & , \alpha_g > 0.85 \end{cases} \tag{13}$$

2.2. Kinetic-frictional theory for granular flow models

In order to have a mathematical closure, the two-phase model, as it is presented, lacks of an interpretation for the solid phase rheology. The kinetic and frictional theories for granular flow seeks to provide a modeling for the rheologic parameters relying on the various states of particles concentration.

For low concentration, the dynamic of the particles is modeled by the kinetic theory for granular flow [13–15] based on the kinetic theory of dense gases presented by Chapman and Cowling [16], where uniform spherical particles are assumed and only instantaneous binary collisions are considered. For this regime, the granular phase properties are defined as functions of the granular temperature θ, which verifies the following energy balance equation:

$$\frac{3}{2}\left[\frac{\partial}{\partial t}(\rho_s\alpha_s\theta) + \nabla\cdot(\rho_s\alpha_s\mathbf{u}_s\theta)\right] = (\boldsymbol{\tau}_s - p_s\mathbf{I}) : \nabla\mathbf{u}_s + \nabla\cdot(\kappa_s\nabla\theta) - \gamma_s + J_v + J_s \tag{14}$$

where κ_s represents the conductivity of granular temperature, γ_s the dissipation of granular energy due to particles collisions, J_v the dissipation due to viscous damping and J_s the production of granular energy due to slip between gas and particles.

For high concentration, rubbing and friction between particles may occur and the phenomena is modeled by the frictional theory. In these regimes, an additive approach is usually adopted, where both frictional and kinetic contributions are considered [20]. Thus, the particle pressure and viscosity are defined as:

$$\mu_s = \mu_{s,\mathrm{KTGF}} + \mu_{s,\mathrm{FRIC}} \tag{15}$$

$$p_s = p_{s,\mathrm{KTGF}} + p_{s,\mathrm{FRIC}} \tag{16}$$

For the kinetic regime, the parameters are modeled following the works of Gidaspow [15] and Lun et al. [14]:

$$\mu_{s,\mathrm{KTGF}} = \frac{10\rho_s d_p\sqrt{\theta\pi}}{96g_0(1+e)}\left[1 + \frac{4}{5}(1+e)\alpha_s g_0\right]^2 + \frac{4}{5}\alpha_s^2\rho_s d_p g_0(1+e)\sqrt{\frac{\theta}{\pi}} \tag{17}$$

$$p_{s,\mathrm{KTGF}} = \rho_s\alpha_s\theta + 2\rho_s\alpha_s^2 g_0(1+e)\theta \tag{18}$$

$$\lambda_s = \frac{4}{3}\rho_s\alpha_s^2 d_p g_0(1+e)\left(\frac{\theta}{\pi}\right)^{1/2} \tag{19}$$

$$\kappa_s = \frac{150\rho_s d_p\sqrt{\theta\pi}}{384g_0(1+e)}\left[1 + \frac{6}{5}(1+e)\alpha_s g_0\right]^2 + 2\alpha_s^2\rho_s d_p g_0(1+e)\sqrt{\frac{\theta}{\pi}} \tag{20}$$

$$\gamma_s = 3(1-e^2)\alpha_s^2\rho_s g_0\theta\left[\frac{4}{d_p}\sqrt{\frac{\theta}{\pi}} - \nabla\cdot\mathbf{u}_s\right] \tag{21}$$

$$J_v = -3K_{sg}\theta \tag{22}$$

$$J_s = K_{sg}\left[3\theta - \frac{K_{sg}d_p(\mathbf{u}_g - \mathbf{u}_s)^2}{4\alpha_s\rho_s\sqrt{\theta\pi}}\right] \tag{23}$$

where e is the restitution coefficient, d_p is the particles diameter and g_0 is the radial distribution. For this last parameter, the Carnahan–Starling model [45] is adopted, where:

$$g_0 = \frac{1}{1-\alpha_s} + \frac{3\alpha_s}{2(1-\alpha_s)^2} + \frac{\alpha_s^2}{2(1-\alpha_s)^3} \tag{24}$$

It should be taken into account that this model is independent of the maximum packing $\alpha_{s,\,\max}$. Therefore, the use of a frictional model is essential to strictly fulfill the maximum packing condition without incurring into numerical manipulation.

The frictional contribution to the particles rheology may be modeled following the works of Schaeffer [19] and Syamlal et al. [39]:

$$\mu_{s,\mathrm{FRIC}} = 0.5p_{s,\mathrm{FRIC}}(I_{2D})^{-1/2}sin(\phi_f) \tag{25}$$

$$p_{s,\mathrm{FRIC}} = 10^{25}(\alpha_s - \alpha_{s,\min})^{10} \tag{26}$$

where ϕ_f is the angle of internal friction and I_{2D} is the second invariant of the deviator of the strain rate tensor. The minimal phase fraction $\alpha_{s,\,\min}$ at which the frictional effects occur is usually set at 0.61.

The Johnson–Jackson model [20] defines:

$$\mu_{s,\mathrm{FRIC}} = 0.5p_{s,\mathrm{FRIC}}sin(\phi_f) \tag{27}$$

$$p_{s,\mathrm{FRIC}} = Fr\frac{(\alpha_s - \alpha_{s,\min})^{\eta}}{(\alpha_{s,\max} - \alpha_s)^{P}} \tag{28}$$

here the $\alpha_{s,\min} = 0.5$. The empirical coefficients are set at $Fr = 0.05$, $\eta = 2$, $P = 5$.

Another commonly used model is the Srivastava and Sundaresan model [21], which differs from the Johnson–Jackson model in the definition of the solid viscosity:

$$\mu_{s,\mathrm{FRIC}} = 0.5p_{s,\mathrm{FRIC}}(I_{2D}^{*})^{-1/2}sin(\phi_f) \tag{29}$$

where $I_{2D}^{*} = I_{2D} + \frac{\theta}{d_p}$

3. Numerical treatment

The model equations are solved using the finite volume method with both phases treated under an incompressible flow hypothesis [46,47] and a combination of the SIMPLE [40] and PISO [41] methods for the pressure–velocity coupling. The algorithm is implemented on the OpenFOAM® platform [34] based on the general structure of the `twoPhaseEulerFoam` solver and the work of Passalacqua et al. [31].

Eqs. (1)–(4) are rewritten taking out the constant phase densities out of the derivative operators and combining both phase continuity equations. Thus, the following system of equations is obtained:

$$\frac{\partial\alpha_s}{\partial t} + \nabla\cdot(\alpha_s\mathbf{u}_s) = 0 \tag{30}$$

$$\alpha_g = 1 - \alpha_s \tag{31}$$

$$\frac{\partial}{\partial t}(\alpha_s \mathbf{u}_s) + \nabla \cdot (\alpha_s \mathbf{u}_s \mathbf{u}_s) = -\frac{\alpha_s}{\rho_s}\nabla p - \frac{1}{\rho_s}\nabla p_s + \nabla \cdot (\alpha_s \boldsymbol{\tau}_s) + \alpha_s \mathbf{g} + \frac{K_{sg}}{\rho_s}(\mathbf{u}_g - \mathbf{u}_s) \tag{32}$$

$$\frac{\partial}{\partial t}(\alpha_g \mathbf{u}_g) + \nabla \cdot (\alpha_g \mathbf{u}_g \mathbf{u}_g) = -\frac{\alpha_g}{\rho_g}\nabla p + \nabla \cdot (\alpha_g \boldsymbol{\tau}_g) + \alpha_g \mathbf{g} + \frac{K_{sg}}{\rho_g}(\mathbf{u}_s - \mathbf{u}_g) \tag{33}$$

$$\nabla \cdot (\alpha_s \mathbf{u}_s + \alpha_g \mathbf{u}_g) = 0 \tag{34}$$

where μ_s and p_s are computed according to the kinetic-frictional theory models and the drag coefficient K_{sg} using the drag models presented in the previous section.

The solving sequence may be summarized as follows: compute the phase volume fractions from the solid continuity equation and volume fraction restriction (Eq. (31)), assemble the phase momentum matrices, solve the momentum linear system for an a-priori velocity estimation (momentum predictor step), compute the pressure field derived from a global volumetric flux conservation (Eq. (34)), correct the face fluxes and velocity fields, and iterate until convergence.

3.1. Momentum equation

Eqs. (32) and (33) may be written in a semi-discrete form as presented by Passalacqua et al. [31]:

$$A_s \mathbf{u}_s = \mathbf{H}_s - \frac{\alpha_s}{\rho_s}\nabla p - \frac{1}{\rho_s}\nabla p_s + \alpha_s \mathbf{g} + \frac{K_{sg}}{\rho_s}(\mathbf{u}_g - \mathbf{u}_s) \tag{35}$$

$$A_g \mathbf{u}_g = \mathbf{H}_g - \frac{\alpha_g}{\rho_g}\nabla p + \alpha_g \mathbf{g} + \frac{K_{sg}}{\rho_g}(\mathbf{u}_s - \mathbf{u}_g) \tag{36}$$

where the matrix $\mathbf{H}_i$ includes the off-diagonal implicit contributions of the advective and diffusive terms, and the explicit contribution of the transient term. The matrix A_i includes the diagonal contributions of the same terms.

It should be remarked that the discretization practice based on the finite volume method involves the calculation of face-centered volumetric fluxes, which are defined as:

$$\varphi_i = \mathbf{u}_{i,f} \cdot \mathbf{S} \tag{37}$$

where i is the phase index and the subscript f indicates a face interpolated value.

Moreover, each phase flux may be expressed a sum of various contributions, as:

$$\varphi_i = \varphi_i^{\mathrm{S}} + \varphi_i^{\mathrm{C}} + \varphi_i^{\mathrm{P}} + \varphi_i^{\mathrm{PP}} + \varphi_i^{\mathrm{G}} \tag{38}$$

where the superscript S represents the same phase velocity contribution, C represents the complementary phase velocity contribution, P represents the shared pressure contribution, PP represents the particle pressure contribution and G represents the gravity contribution.

The are many ways to enforce the link between phases through the drag force term [35]. In this work, the attention will be focused in two widely adopted methods following the nomenclature of Karema et al. [38]: the *partially implicit method* (PIM) and the *partial elimination algorithm* (PEA).

The PIM relies on treating the i-phase velocity of the i-phase drag term implicitly. This means that the cell-centered phase velocities are computed as:

$$\mathbf{u}_{s,\mathrm{PIM}} = \zeta_s\left(\mathbf{H}_s + \frac{K_{sg}}{\rho_s}\mathbf{u}_g - \frac{\alpha_s}{\rho_s}\nabla p - \frac{1}{\rho_s}\nabla p_s + \alpha_s \mathbf{g}\right) \tag{39}$$

$$\mathbf{u}_{g,\mathrm{PIM}} = \zeta_g\left(\mathbf{H}_g + \frac{K_{sg}}{\rho_g}\mathbf{u}_s - \frac{\alpha_g}{\rho_g}\nabla p + \alpha_g \mathbf{g}\right) \tag{40}$$

where

$$\zeta_i = \frac{1}{A_i + \dfrac{K_{sg}}{\rho_i}} \tag{41}$$

Here, the gradient of the particle pressure is rewritten as:

$$\nabla p_s = \left(\frac{\partial p_s}{\partial \alpha_s}\right)\nabla \alpha_s \tag{42}$$

for the numerical handling. The dependence of p_s with θ is omitted for the derivation of Eq. (42).

According to Eqs. (37)–(40), the flux contributions are:

$$\varphi^{\mathrm{S}}_{s,\mathrm{PIM}} = \zeta_{s,f}\mathbf{H}_{s,f} \cdot \mathbf{S} \tag{43}$$

$$\varphi^{\mathrm{S}}_{g,\mathrm{PIM}} = \zeta_{g,f}\mathbf{H}_{g,f} \cdot \mathbf{S} \tag{44}$$

$$\varphi^{\mathrm{C}}_{s,\mathrm{PIM}} = \zeta_{s,f}\left(\frac{K_{sg}}{\rho_s}\right)_f \varphi^0_g \tag{45}$$

$$\varphi^{\mathrm{C}}_{g,\mathrm{PIM}} = \zeta_{g,f}\left(\frac{K_{sg}}{\rho_g}\right)_f \varphi^0_s \tag{46}$$

$$\varphi^{\mathrm{P}}_{s,\mathrm{PIM}} = -\zeta_{s,f}\left(\frac{\alpha_s}{\rho_s}\right)_f \nabla p \cdot \mathbf{S} \tag{47}$$

$$\varphi^{\mathrm{P}}_{g,\mathrm{PIM}} = -\zeta_{g,f}\left(\frac{\alpha_g}{\rho_g}\right)_f \nabla p \cdot \mathbf{S} \tag{48}$$

$$\varphi^{\mathrm{PP}}_{s,\mathrm{PIM}} = -\zeta_{s,f}\left(\frac{1}{\rho_s}\frac{\partial p_s}{\partial \alpha_s}\right)_f \nabla \alpha_s \cdot \mathbf{S} \tag{49}$$

$$\varphi^{\mathrm{PP}}_{g,\mathrm{PIM}} = 0 \tag{50}$$

$$\varphi^{\mathrm{G}}_{s,\mathrm{PIM}} = \zeta_{s,f}\alpha_{s,f}\mathbf{g} \cdot \mathbf{S} \tag{51}$$

$$\varphi^{\mathrm{G}}_{g,\mathrm{PIM}} = \zeta_{g,f}\alpha_{g,f}\mathbf{g} \cdot \mathbf{S} \tag{52}$$

where $\mathbf{S}$ represents the face normal vector and the superscript 0 indicates the stored fields from a previous iteration.

The final expression for the phase fluxes is obtained by including each contribution to Eq. (38). This coupling method is currently implemented in the official distribution of OpenFOAM®[34]

On the other hand, the PEA incorporates the velocity obtained in Eq. (39) into Eq. (36) and Eq. (40) into Eq. (35). This leads to another expression for the cell-centered velocities given by:

$$\mathbf{u}_{s,\mathrm{PEA}} = \xi_s\left\{\mathbf{H}_s + \frac{K_{sg}\zeta_g}{\rho_s}\mathbf{H}_g - \left[\frac{\alpha_s}{\rho_s} + \frac{K_{sg}\alpha_g\zeta_g}{\rho_g\rho_s}\right]\nabla p - \frac{1}{\rho_s}\nabla p_s + \left[\alpha_s + \frac{K_{sg}\alpha_g\zeta_g}{\rho_s}\right]\mathbf{g}\right\} \tag{53}$$

$$\mathbf{u}_{g,\mathrm{PEA}} = \xi_g\left\{\mathbf{H}_g + \frac{K_{sg}\zeta_s}{\rho_g}\mathbf{H}_s - \left[\frac{\alpha_g}{\rho_g} + \frac{K_{sg}\alpha_s\zeta_s}{\rho_s\rho_g}\right]\nabla p - \frac{K_{sg}\zeta_s}{\rho_s\rho_g}\nabla p_s + \left[\alpha_g + \frac{K_{sg}\alpha_s\zeta_s}{\rho_g}\right]\mathbf{g}\right\} \tag{54}$$

where

$$\xi_i = \frac{1}{A_i + \frac{K_{sg}}{\rho_i} - \frac{K_{sg}^2\zeta_j}{\rho_i\rho_j}} \tag{55}$$

and j represents the complementary phase of the phase i.

For this method, the flux contributions are:

$$\varphi^{S}_{s,\mathrm{PEA}} = \xi_{s,f}\mathbf{H}_{s,f}\cdot\mathbf{S} \tag{56}$$

$$\varphi^{S}_{g,\mathrm{PEA}} = \xi_{g,f}\mathbf{H}_{g,f}\cdot\mathbf{S} \tag{57}$$

$$\varphi^{C}_{s,\mathrm{PEA}} = \xi_{s,f}\left(\frac{K_{sg}\lambda_g}{\rho_s}\mathbf{H}_g\right)_f\cdot\mathbf{S} \tag{58}$$

$$\varphi^{C}_{g,\mathrm{PEA}} = \xi_{g,f}\left(\frac{K_{sg}\lambda_s}{\rho_g}\mathbf{H}_s\right)_f\cdot\mathbf{S} \tag{59}$$

$$\varphi^{P}_{s,\mathrm{PEA}} = -\xi_{s,f}\left(\frac{\alpha_s}{\rho_s}+\frac{K_{sg}\alpha_g\lambda_g}{\rho_g\rho_s}\right)_f\nabla p\cdot\mathbf{S} \tag{60}$$

$$\varphi^{P}_{g,\mathrm{PEA}} = -\xi_{g,f}\left(\frac{\alpha_g}{\rho_g}+\frac{K_{sg}\alpha_s\lambda_s}{\rho_s\rho_g}\right)_f\nabla p\cdot\mathbf{S} \tag{61}$$

$$\varphi^{PP}_{s,\mathrm{PEA}} = -\xi_{s,f}\left(\frac{1}{\rho_s}\frac{\partial p_s}{\partial\alpha_s}\right)_f\nabla\alpha_s\cdot\mathbf{S} \tag{62}$$

$$\varphi^{PP}_{g,\mathrm{PEA}} = -\xi_{g,f}\left(\frac{K_{sg}\lambda_s}{\rho_s\rho_g}\frac{\partial p_s}{\partial\alpha_g}\right)_f\nabla\alpha_g\cdot\mathbf{S} \tag{63}$$

$$\varphi^{G}_{s,\mathrm{PEA}} = \xi_{s,f}\left(\alpha_s+\frac{K_{sg}\alpha_g\lambda_g}{\rho_s}\right)_f\mathbf{g}\cdot\mathbf{S} \tag{64}$$

$$\varphi^{G}_{g,\mathrm{PEA}} = \xi_{g,f}\left(\alpha_g+\frac{K_{sg}\alpha_s\lambda_s}{\rho_g}\right)_f\mathbf{g}\cdot\mathbf{S} \tag{65}$$

The PEA is based on the work of Spalding [36] and the complete derivation of these expressions is detailed in the work of Passalacqua et al. [31]. It has the advantage of achieving a decoupling of each phase velocity from its complementary phase, which favors the momentum convergence for drag dominated problems [35]. Many authors have adopted this method [31,39,48] and its convergence rate and stability conditions have been investigated [37,38].

3.2. Pressure equation

The pressure equation is derived from the incompressibility condition (Eq. (34)), which is rewritten in a discrete form as:

$$\sum_f \varphi = 0 \tag{66}$$

where φ is the global flux defined as:

$$\varphi = \alpha_{s,f}\varphi_s + \alpha_{g,f}\varphi_g \tag{67}$$

Replacing φ_s and φ_g by Eq. (38), using Eqs. (43)–(52) (or Eqs. (56)–(65) for the PEA) and taking into account that Eqs. (47) and (48) (or Eqs. (60) and (61)) have terms involving ∇p, the pressure equation is expressed as:

$$\sum_f\left[D^{P}(\nabla p\cdot\mathbf{S})\right] = \sum_f\left(\alpha_{s,f}\hat{\varphi}_s+\alpha_{g,f}\hat{\varphi}_g\right) \tag{68}$$

where

$$D^{P}_{\mathrm{PIM}} = -\left[\alpha_{s,f}\zeta_{s,f}\left(\frac{\alpha_s}{\rho_s}\right)_f+\alpha_{g,f}\zeta_{g,f}\left(\frac{\alpha_g}{\rho_g}\right)_f\right] \tag{69}$$

$$D^{P}_{\mathrm{PEA}} = -\left[\alpha_{s,f}\xi_{s,f}\left(\frac{\alpha_s}{\rho_s}+\frac{K_{sg}\alpha_g\zeta_g}{\rho_g\rho_s}\right)_f+\alpha_{g,f}\xi_{g,f}\left(\frac{\alpha_g}{\rho_g}+\frac{K_{sg}\alpha_s\zeta_s}{\rho_s\rho_g}\right)_f\right] \tag{70}$$

and

$$\hat{\varphi}_i = \varphi^{S}_i+\varphi^{C}_i+\varphi^{PP}_i+\varphi^{G}_i \tag{71}$$

The matrices $\mathbf{H}_s$ and $\mathbf{H}_g$ needed to compute $\hat{\varphi}_s$ and $\hat{\varphi}_g$ in Eq. (71) are calculated by approximating the velocity field from previously stored pressure fields. This step is known as the *momentum predictor*. The predicted velocity fields are obtained by solving the following system:

$$A^{*}_s\mathbf{u}_s = \mathbf{H}^{*}_s+\mathcal{R}\left[\alpha_{s,f}\mathbf{g}\cdot\mathbf{S}-\left(\frac{\alpha_s}{\rho_s}\right)_f\nabla p^0\cdot\mathbf{S}-\left(\frac{1}{\rho_s}\frac{\partial p_s}{\partial\alpha_s}\right)_f\nabla\alpha_s\cdot\mathbf{S}\right] \tag{72}$$

$$A^{*}_g\mathbf{u}_g = \mathbf{H}^{*}_g+\mathcal{R}\left[\alpha_{g,f}\mathbf{g}\cdot\mathbf{S}-\left(\frac{\alpha_g}{\rho_g}\right)_f\nabla p^0\cdot\mathbf{S}\right] \tag{73}$$

where

$$A^{*}_i = A_i+\frac{K_{sg}}{\rho_i} \tag{74}$$

$$\mathbf{H}^{*}_i = \mathbf{H}_i+\frac{K_{sg}}{\rho_i}\mathbf{u}_j \tag{75}$$

and $\mathcal{R}[\ldots]$ is the reconstruction operator of the face-interpolated fields to cell-centered values. The reader should notice that the momentum predictors preserve the same form for both coupling methods considered, but, for the PEA, the implicit part of the drag term contribution must be included after the calculation of the coefficients ξ_i and ζ_i.

With the updated values of the pressure field, each phase flux is corrected according to:

$$\varphi_{i,\mathrm{PIM}} = \hat{\varphi}_{i,\mathrm{PIM}}-\alpha_{i,f}\zeta_{i,f}\left(\frac{\alpha_i}{\rho_i}\right)_f\nabla p\cdot\mathbf{S} \tag{76}$$

or

$$\varphi_{i,\mathrm{PEA}} = \hat{\varphi}_{i,\mathrm{PEA}}-\alpha_{i,f}\xi_{i,f}\left(\frac{\alpha_i}{\rho_i}+\frac{K_{sg}\alpha_j\zeta_j}{\rho_i\rho_j}\right)_f\nabla p\cdot\mathbf{S} \tag{77}$$

In order to ensure consistency in the correction of the cell-centered velocity fields, Passalacqua et al. pointed out the need to reconstruct the phase fluxes with the use of cell-centered coefficients. For the PIM, the corrected cell-centered velocity is:

$$\mathbf{u}_{i,\mathrm{PIM}} = \mathbf{u}^{0}_{i,\mathrm{PIM}}+\zeta_i\mathcal{R}\left[\frac{\varphi_i-\hat{\varphi}_i}{\zeta_{i,f}}\right] \tag{78}$$

The procedure for the PEA is not so straightforward since both ξ_i and ζ_i coefficients must be used in its cell-centered form for the velocity correction. This leads to the following expressions:

$$\begin{aligned}\mathbf{u}_{s,\mathrm{PEA}} = \mathbf{u}^{0}_{s,\mathrm{PEA}}+\xi_s\Bigg\{&\mathcal{R}\left[\alpha_{s,f}\mathbf{g}\cdot\mathbf{S}-\left(\frac{\alpha_s}{\rho_s}\right)_f\nabla p\cdot\mathbf{S}\right]\\&-\mathcal{R}\left[\left(\frac{1}{\rho_s}\frac{\partial p_s}{\partial\alpha_s}\right)_f\nabla\alpha_s\cdot\mathbf{S}\right]\\&+\frac{K_{sg}\zeta_g}{\rho_s}\mathcal{R}\left[\alpha_{g,f}\mathbf{g}\cdot\mathbf{S}-\left(\frac{\alpha_g}{\rho_g}\right)_f\nabla p\cdot\mathbf{S}\right]\Bigg\}\end{aligned} \tag{79}$$

$$\begin{aligned}\mathbf{u}_{g,\mathrm{PEA}} = \mathbf{u}^{0}_{g,\mathrm{PEA}}+\xi_g\Bigg\{&\mathcal{R}\left[\alpha_{g,f}\mathbf{g}\cdot\mathbf{S}-\left(\frac{\alpha_g}{\rho_g}\right)_f\nabla p\cdot\mathbf{S}\right]\\&-\frac{K_{sg}\zeta_s}{\rho_s}\mathcal{R}\left[\left(\frac{1}{\rho_g}\frac{\partial p_s}{\partial\alpha_g}\right)_f\nabla\alpha_g\cdot\mathbf{S}\right]\\&+\frac{K_{sg}\zeta_s}{\rho_g}\mathcal{R}\left[\alpha_{s,f}\mathbf{g}\cdot\mathbf{S}-\left(\frac{\alpha_s}{\rho_s}\right)_f\nabla p\cdot\mathbf{S}\right]\Bigg\}\end{aligned} \tag{80}$$

3.3. Continuity equation

Since Eq. (30) must be verified locally for each time step, it is unnecessary to solve both phase continuity equations. Instead, the disperse phase continuity equation is solved and the volume fraction of the remaining phase is derived from Eq. (31). Thus, Eq. (30) can be written in a semi-discrete form as:

$$\frac{\partial \alpha_s}{\partial t} + \sum_f \alpha_{s,f}\varphi_s = 0 \tag{81}$$

where the solid phase flux may be expressed in terms of a global phase flux φ and a relative flux $\varphi_{r,s}$ as:

$$\varphi_s = \varphi + \alpha_{g,f}\varphi_{r,s} \tag{82}$$

and

$$\varphi_{r,s} = \varphi_s - \varphi_g \tag{83}$$

Recalling Eqs. (38), (67) and (83), the global and relative flux are rewritten as:

$$\varphi = \alpha_{s,f}\breve{\varphi}_s + \alpha_{s,f}\varphi_s^{PP} + \alpha_{g,f}\breve{\varphi}_g + \alpha_{g,f}\varphi_g^{PP} \tag{84}$$

$$\varphi_{r,s} = \breve{\varphi}_s + \varphi_s^{PP} - \breve{\varphi}_g - \varphi_g^{PP} \tag{85}$$

where

$$\breve{\varphi}_i = \varphi_i^S + \varphi_i^C + \varphi_i^P + \varphi_i^G \tag{86}$$

Then, using Eqs. (84) and (85), Eq. (82) becomes:

$$\varphi_s = \breve{\varphi} + \alpha_{g,f}\breve{\varphi}_{r,s} + \varphi_s^{PP} \tag{87}$$

where

$$\breve{\varphi} = \alpha_{s,f}\breve{\varphi}_s + \alpha_{g,f}\breve{\varphi}_g \tag{88}$$

$$\breve{\varphi}_{r,s} = \breve{\varphi}_s - \breve{\varphi}_g \tag{89}$$

Finally, Eq. (87) may be included in Eq. (81) leading to the following semi-discrete form of the phase continuity equation:

$$\frac{\partial \alpha_s}{\partial t} + \sum_f \alpha_{s,f}\breve{\varphi} + \sum_f \alpha_{s,f}\alpha_{g,f}\breve{\varphi}_{r,s} - \sum_f D_i^{PP}\nabla\alpha_s \cdot \mathbf{S} = 0 \tag{90}$$

where

$$D_{i,\mathrm{PIM}}^{PP} = -\zeta_{s,f}\left(\frac{1}{\rho_s}\frac{\partial p_s}{\partial \alpha_s}\right)_f \tag{91}$$

$$D_{i,\mathrm{PEA}}^{PP} = -\xi_{s,f}\left(\frac{1}{\rho_s}\frac{\partial p_s}{\partial \alpha_s}\right)_f \tag{92}$$

Here, the fourth term on Eq. (90) is arranged to represent the diffusion of the particles fraction with a particle pressure-dependent diffusivity. The bounding of the phase fraction between zero and one is achieved using an operator splitting technique where the first three terms are solved as a pure transport equation and the effect of the particle pressure is added implicitly. This procedure is based on the work of Weller [30] and Passalacqua et al. [31].

The solution of the transport terms relies on the MULES integrator [42,43], which is a flux corrected transport-based scheme [44] and guarantees that the solution will be bounded between the global extreme values. If the extremes are selected to be [0, 1], the maximum packing limit must be enforced by the physical models. But, if the extremes are selected to be [0, $\alpha_{s,\,\max}$] then the MULES integrator will bound the values towards the packing limit.

The upper limit for α_s imposed through MULES is subject of discussion. If the upper limit is set at $\alpha_{s,\,\max}$, this condition will be satisfied rigorously and much will be gained from a stability point of view, but the physical effect of the kinetic-frictional model on the packing limit will be mixed up with the limits imposed numerically. In this work, efforts were made to increase the numerical stability by strictly imposing the bounding limits for α_s at [0, 1] with MULES and leaving the maximum packing condition to be handled by the kinetic-frictional models.

3.4. Granular energy equation

The mathematical closure of the two-phase system relies on the definition of μ_s and p_s. These parameters are modeled based on an additive approach of the kinetic and frictional contributions. The kinetic contribution is related to the granular energy field which verifies a balance equation given by Eq. (14). This equation may be rewritten in a form that is consistent with the numerical treatment:

$$A(\theta) = B(\theta) \tag{93}$$

$$A(\theta) = \frac{\partial}{\partial t}\left(\frac{3}{2}\rho_s\alpha_s\theta\right) + \nabla\cdot\left(\frac{3}{2}\rho_s\alpha_s\mathbf{u}_s\theta\right) \tag{94}$$

$$B(\theta) = \nabla\cdot(\kappa_s\nabla\theta) + [(-\tilde{p}_s\mathbf{I}:\nabla\mathbf{u}_s) - \tilde{\gamma}_s - \tilde{J}_v + \tilde{J}_s]\theta + (\tau_s:\nabla\mathbf{u}_s) \tag{95}$$

where $\tilde{\phi} = \dfrac{\phi}{\theta}$ and ϕ is a generic parameter.

It should be noticed that the first term on the right-hand-side of Eq. (14) is split for the numerical treatment. This generates a granular energy dissipation term due to shear stress, which is treated explicitly (last term on Eq. (95)), and a granular energy dissipation term due to normal stress, which is treated implicitly as a reactive term (first term of the square brackets on Eq. (95)). Added to this, the other dissipative terms γ_s, J_v and J_s are also treated as reactive terms for the numerical implementation.

In many applications, the dissipation due to inelastic collisions γ_s tends to dominate the dissipation-production phenomena near the packing limit. Due to its negative sign, $\tilde{\gamma}_s$ has a stabilizing effect on the numerical solution, being:

$$\tilde{\gamma}_s = 3(e^2-1)\alpha_s^2\rho_s g_0\left[\frac{4}{d_p}\left(\frac{\theta^0}{\pi}\right)^2 - \nabla\cdot\mathbf{u}_s\right] \tag{96}$$

It is clear, from Eq. (96), that special care should be taken when the restitution coefficient $e \to 1$ since $\tilde{\gamma}_s \to 0$ and an off-diagonal dominance trend may arise in the discrete matrix. In order to avoid this, a switching scheme treatment is adopted. This treatment consists on setting a maximum restitution coefficient ($e_{\max}$) above which numerical instabilities are expected. If the real restitution coefficient of the problem is below this maximum value, the solution procedure is straightforward. On the other hand, if the restitution coefficient is above the maximum value, then a diffusive term is added implicitly and subtracted explicitly. The coefficient corresponding to this term is:

$$\tilde{\gamma}_s^m = 3(e_{\max}^2-1)\alpha_s^2\rho_s g_0\left[\frac{4}{d_p}\left(\frac{\theta^0}{\pi}\right)^2 - \nabla\cdot\mathbf{u}_s\right] \tag{97}$$

Then, the granular energy equation becomes:

$$A(\theta) = B(\theta) + \tilde{\gamma}_s^m(\theta^0 - \theta) \tag{98}$$

Therefore, the numerical difficulties of having small values of $\tilde{\gamma}_s$ are avoided by adding extra numerical diffusivity with no disturbance on the calculation of θ.

3.5. The PIMPLE algorithm

The PIMPLE algorithm is a combination of the SIMPLE [40] and PISO [41] methods, which allows the coupling between phases and the use of under-relaxation factors to enforce the convergence of the iterative procedure. The sequence consists of the following steps:

1. Read the physical and numerical parameters, boundary conditions and previously stored field
2. Start the PIMPLE loop and iterate until convergence
   (a) Start the continuity equation loop and iterate until convergence
      i. Solve the solid phase continuity equation (Eq. (90)) using the MULES integrator without the particle pressure flux contribution.
      ii. Include the particle pressure flux contribution implicitly
      iii. Relax the continuity equation and solve for α_s, then compute α_g
   (b) Compute K_{sg} according to the selected drag model
   (c) Compute the granular energy equation coefficients
   (d) Relax and solve the granular energy equation (Eq. (98))
   (e) Compute μ_s and p_s according to the selected kinetic-frictional models
   (f) Construct each phase momentum matrix
   (g) Relax, add the explicit terms and solve the momentum linear system for the phase velocity predictors (Eqs. (72) and (73))
   (h) Start the pressure corrector loop and iterate until convergence
      i. Interpolate the momentum matrix coefficients and the phase fraction fields on cell faces
      ii. Construct the right-hand-side and the pressure diffusion coefficient of the pressure equation
      iii. Start the non-orthogonal correction loop and iterate a predefined number of times
         (1) Construct and solve the pressure equation (Eq. (68))
      iv. Add the pressure contribution and correct the phase fluxes (Eq. (76) and (77))
      v. Relax the pressure field
      vi. Reconstruct the cell-centered phase velocities (Eqs. (78), (79) and (80))
3. Restart the sequence for the next time-step.

4. Validation tests

The following test cases are selected to study the numerical performance of the solver. First, a one-dimensional particles settling simulation is carried out. Some numerical challenging conditions arise at the limits of maximum packing and phase disappearance. Secondly, a two-dimensional bubbling fluidized bed problem is addressed. Here, the time-averaged particles distribution is compared with the results of the literature.

4.1. Particles settling

This test consists of a vertical tube with a uniformly distributed concentration of particles which, under the effect of gravity, start to settle at the bottom (Fig. 1). The tube has a height of 0.3 m with an initial concentration of solids of 0.3. The gas density is 1.2 kg/m^3 with a dynamic viscosity of 1.8×10^{-5} Pa s, while the solid phase is constituted by particles of 0.4 mm of diameter, has a density of 2000 kg/m^3 and a restitution coefficient of 0.6. The Gidaspow drag model is used and the granular energy balance equation is solved along with the Schaeffer frictional model.

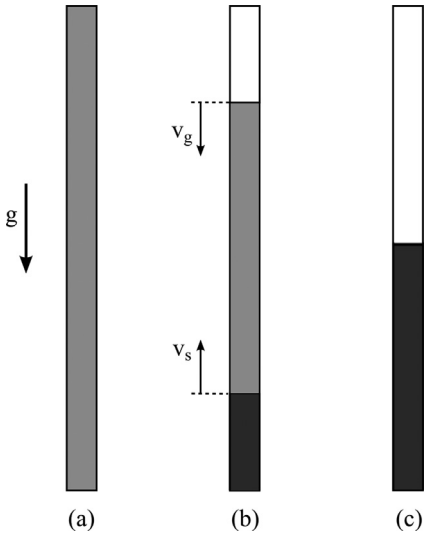

Fig. 1. (a) Uniformly distributed mixture of particles and gas. (b) A transient state with pure gas at the top, maximum particles packing at the bottom and mixture in the middle. (c) Fully settled state with complete segregation of pure gas and particles at maximum packing condition.

The problem is discretized using 30 uniform cells and a time step of 1×10^{-4} s. A second order scheme is used for the time discretization, while a second order upwind is used for the divergence terms interpolation. Maximum residuals of 1×10^{-4} and 1×10^{-7} are allowed for the momentum and continuity equations respectively. This is achieved with 20 PIMPLE loop iterations and 3 pressure iterations per time step. No significant difference was found in the convergence rate using both drag coupling methods.

In Fig. 2 results for three stages of the settling are presented and compared with the results obtained by Passalacqua et al. [31]. A good level of agreement was achieved with stable transitions and a complete segregation of phases was reached at $t = 0.25$ s.

The distribution of particles at the settled state is related to the range of applicability of the frictional effects given by the corresponding model. In this case, the Schaffer model was adopted in which the frictional effects occur at $\alpha_{s,\min} = 0.61$. This produces a nearly constant distribution of particles at the bottom of the tube. Whereas, if the Johnson–Jackson model had been used with $\alpha_{s,\min} = 0.5$, the solids distribution would have a smooth variation at the middle of the tube. This behavior could also be predicted by assuming a force balance at the settled state given by:

$$\frac{\partial (p_{s,\mathrm{FRIC}})}{\partial y} = \frac{\partial (p_{s,\mathrm{FRIC}})}{\partial \alpha_s} \frac{\partial \alpha_s}{\partial y} \simeq \rho_s \alpha_s g \tag{99}$$

here the forces given by the shared pressure and the kinetic contribution to the particle pressure have been neglected.

The results of solving Eq. (99) for a prescribed volume fraction of $\alpha_s = 0.3$ at $y = 0.15$ m are shown in Fig. 3.

Regarding the onset of the phase settling at both ends of the tube, the MULES integrator was modified from the original distribution of OpenFOAM®. This was done to allow local maximum values for problems with phase accumulation [43,49,50]. In this particular case, it is expected that the first cell at the bottom of the tube presents an increasing value of the solid volume fraction field until the maximum packing is achieved.

4.2. Bubbling fluidized bed

A two-dimensional bubbling fluidized bed problem with Geldart B particles based on the experimental setup of Makkawi et al. [4] is studied (Fig. 4). All the system parameters, models adopted and dimensions are summarized in Table 1.

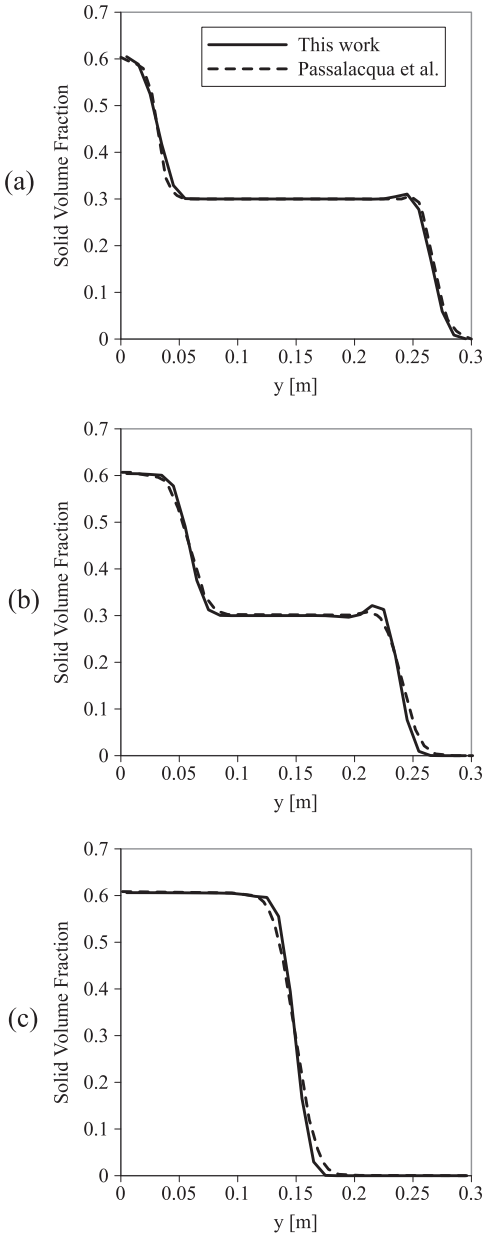

Fig. 2. (a) Solid fraction distribution along the tube height at $t = 0.1$ s, (b) at $t = 0.15$ s, and (c) at $t = 0.3$ s.

A grid of 14 × 100 cells is adopted to simulate this problem. For this configuration, with Geldart B particles, Parmentier et al. [2] showed that this refinement is high enough to accurately predict the bed expansion and the solid volume fraction profile in the cross-axial direction when compared to the experimental predictions of Makkawi et al. [4].

The Johnson–Jackson boundary conditions [20] are used to describe the behavior of the solid phase in contact with the walls:

$$\frac{\partial \mathbf{u}_{s,w}}{\partial x} = \frac{\pi}{6}\frac{\alpha_{s,w}}{\alpha_{s,\max}}\phi_w \rho_s g_0 \frac{\sqrt{3\theta_w}}{\mu_s}\mathbf{u}_{s,w} \tag{100}$$

$$\frac{\partial \theta_w}{\partial x} = -\frac{\pi}{6}\frac{\alpha_{s,w}}{\alpha_{s,\max}}\phi_w \frac{\rho_s^2}{\kappa_s} g_0 \frac{\sqrt{3\theta_w}}{\mu_s}|\mathbf{u}_{s,w}|^2 + \frac{\pi}{4}\frac{\alpha_{s,w}}{\alpha_{s,\max}}(1-e_w^2)\frac{\rho_s}{\kappa_s} g_0 \sqrt{3\theta_w^3} \tag{101}$$

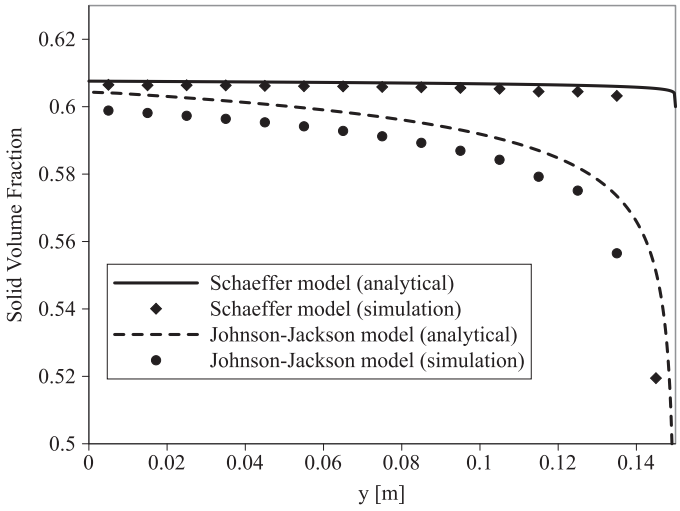

Fig. 3. Numerical and analytical predictions of the volume fraction profiles at the settled state for different frictional models.

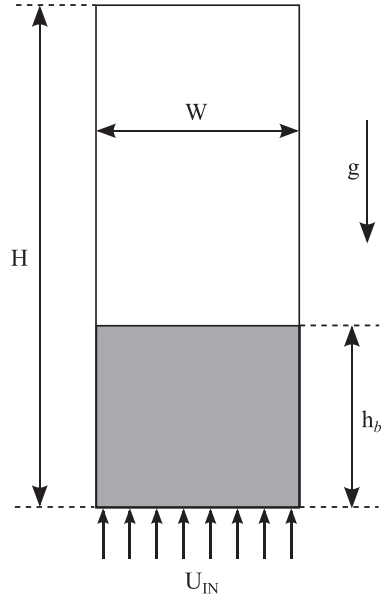

Fig. 4. Bubbling fluidized bed problem scheme.

Table 1
Bubbling fluidized bed problem general parameters.

Description	Value
Gas density	1.4 kg/m^3
Gas viscosity	1.8×10^{-5} Pa s
Solid density	2500 kg/m^3
Particles diameter	350 μm
Restitution coefficient between particles	0.8
Width (W)	0.138 m
Height (H)	1 m
Bed initial height (h_b)	0.2 m
Grid	14 × 100 cells
Time step	1.0×10^{-4} s
Overall simulation time	30 s
Time discretization	2nd order implicit
Divergence interpolation	limited central difference
Drag model	Gidaspow
Wall solid velocity	Johnson–Jackson BC
Wall granular energy	Johnson–Jackson BC
Vertical inlet gas velocity (U_{IN})	0.54 m/s
Outlet pressure	0 Pa
Initial bed solid fraction	0.58

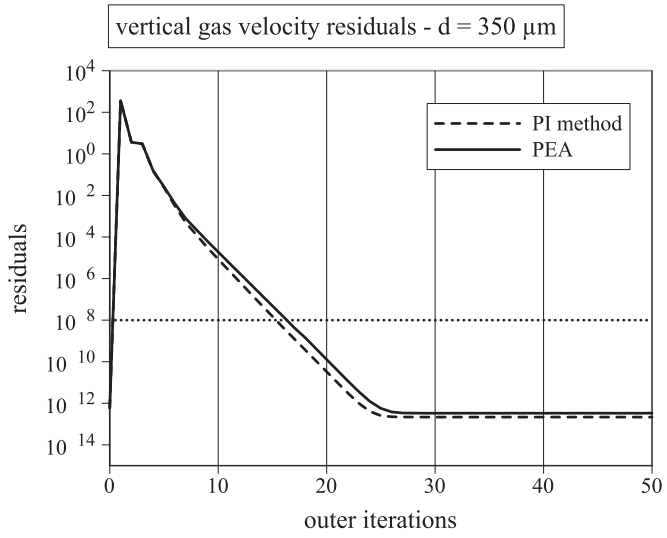

Fig. 5. Convergence rate of the velocity field for both drag coupling methods.

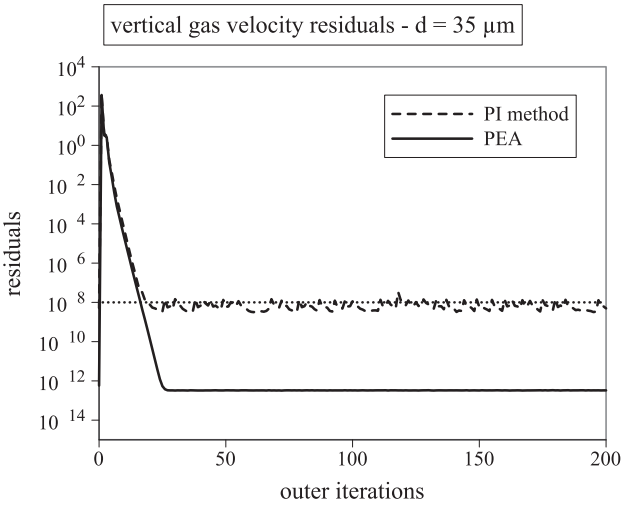

Fig. 6. Convergence rate of the velocity field for both drag coupling methods with $d_p = 35\,\mu$m.

These expressions represent Robin boundary conditions and are usually associated with rough walls, where ϕ_w is the specularity coefficient. The fully slip condition correspond to $\phi_w = 0$, while $\phi_w = 1$ corresponds to very rough walls. The particle-wall restitution coefficient e_w is a measure of how elastic is the collision between particles and the wall, where $e_w = 1$ represents a perfectly elastic collision. Benyahia et al. [51] mentioned the lack of literature reporting realistic values of such coefficients, and its impact on the hydrodynamic behavior of fluidized beds is a current topic of discussion [52]. For the present case, ϕ_w is set at 0.6 which represents intermediate rough walls which may be considered more realistic than the usual slip conditions corresponding to perfectly smooth walls. Also, e_w is taken arbitrarily as 0.8 since it has a small impact on the macroscopic results, such as the averaged solid phase velocity profile and bed height [52].

A maximum allowable value of 1×10^{-8} for the gas phase vertical velocity residuals is taken arbitrarily as a convergence criteria. For the problem conditions, this criteria is met in less than 20 PIMPLE loop iterations. The measure was taken at $t = 0.01$ s after the fluidization start-up and the convergence of the velocity residuals is depicted in Fig. 5. Only a slight difference between both methods is appreciated (around one iteration per time step).

Oliveira et al. [35] showed that, for a one-dimensional air-water fluidized bed problem, the velocity residuals for the PIM and PEA require the same number of iterations to converge, under low to moderate coupling conditions (this behavior is verified in Fig. 5). However, for higher values of the drag coefficient, the PIM fails to converge to the prescribed precision. Karema et al. [38] extended the one-dimensional analysis of Oliveira et al. to a two-dimensional fluidized bed problem and studied the convergence of both methods for low to moderate coupling regimes. They proposed an estimation of the characteristic time scale of the interphase coupling which was used to calculate a non-dimensional drag coefficient similar to the one proposed by Oliveira et al. The time step adopted by Karema et al. for all the studied conditions are below the characteristic time scale of the interphase coupling, therefore, both methods predict reasonably well the coupling between phases.

In the present work, the analysis is advocated to stronger coupling conditions. This is achieved by adopting a smaller particle diameter, which are in the range of practical applications. The use of the particles diameter as a variable parameter has the advantage that, with the exception of some KTGF models, it only affects the calculation of the drag coefficient.

The characteristic time scale is calculated according to the criteria of Karema et al. and the most demanding condition is met at the packed region, where the Ergun model is valid. Therefore, the characteristic time scale (t_{sc}) and non-dimensional drag coefficient ($\overline{C}_d$) are:

$$t_{sc} = \left[150 \frac{\mu_g}{\alpha_{mf} \rho_s d_p^2} + 1.75 \frac{\rho_g u_{mf}}{\rho_s d_p \alpha_{mf}} \right]^{-1} \tag{102}$$

$$\overline{C}_d = \frac{\rho_s u_{mf}}{t_{sc} g (\rho_s - \rho_g)} \tag{103}$$

where the velocity of minimum fluidization $u_{mf} = 0.26$ m/s and the gas volume fraction at minimum fluidization $\alpha_{mf} = 0.39$. For the problem conditions, Eqs. (102) and (103) lead to:

$$t_{sc} = 0.041\text{s},\ \overline{C}_d = 1.66 \tag{104}$$

The time step is still below the characteristic time scale and the non-dimensional drag coefficient is an order of magnitude below the value at which the convergence problems of the PIM arise (as reported by Oliveira et al.). This explains the similar convergence trend of both coupling methods. However, for smaller particles, the drag force magnitude becomes dominant and the convergence of the PIM is compromised, as depicted in Figs. 6 and 7.

For these conditions, the characteristic time scale and drag coefficient are:

$$d_p = 35\mu\text{m} \rightarrow t_{sc} = 4.4 \times 10^{-4}\text{s},\ \overline{C}_d = 154.48 \tag{105}$$

$$d_p = 3.5\mu\text{m} \rightarrow t_{sc} = 4.4 \times 10^{-6}\text{s},\ \overline{C}_d = 15333.5 \tag{106}$$

The first alternative correspond to Geldart A particles ($d_p = 35\ \mu$m and $\rho_s = 2500$ kg/m^3), for which the characteristic time scale is slightly higher than the time step adopted, but the drag coefficient is beyond the limit of 10, which explains the difficulties in the velocity convergence for the PIM. This behavior is emphasized for the extremely fine powder ($d_p = 3.5\ \mu$m), where both the time scale and the drag coefficient are clearly beyond the limit. In these conditions, the PEA requires more than 50 iterations to converge to machine precision, while the PIM cannot converge to the prescribed tolerance. For both particles diameter, a smaller time step is required to achieved convergence with the PIM. However, due

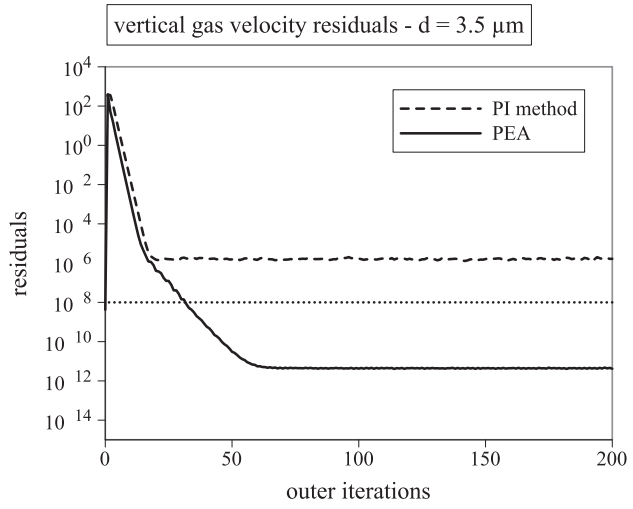

Fig. 7. Convergence rate of the velocity field for both drag coupling methods with $d_p = 3.5$ μm.

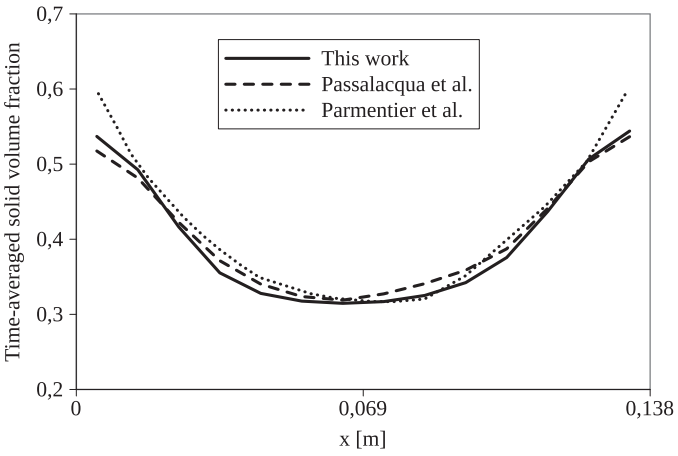

Fig. 8. Time-averaged solid volume fraction profile at $y = 0.16$ m.

to the low scalability for parallel computing of the problem ($\sim 10^3$ to 10^4 cells), the time step reduction makes the adoption of this method unaffordable.

In Fig. 8, time-averaged solid fraction profiles are shown and compared against the simulations of Passalacqua et al. [31] and Parmentier et al. [2] with OpenFOAM® [34] and MFIX® [39] respectively. Here the maximum packing is set at $\alpha_{s,\max} = 0.63$ and the angle of internal friction ϕ_f is set at 28°, while the minimal fraction at which frictional effects occur is $\alpha_{s,\min} = 0.61$ according to the Schaeffer frictional model. The particles distribution was taken at a height of 0.16 m from the bottom of the bed and a time average was done between 10 and 30 s from the start of the simulation to avoid the effects of the fluidization start-up.

The solid vertical velocity profile at $y = 0.16$ m is compared with the simulations performed by Li [53] as it is shown in Fig. 9. The predicted results shows a qualitative agreement with a typical pattern of two counter-rotating loops with particles moving upwards in the center region and a downward recirculation near the walls. Here it is important to remark that, although the original work of Makkawi et al. [4] does not present experimental results for the solid phase velocity, differences may arise in time-averaged solid phase velocity profiles when 2D simulations are compared with pseudo-2D experiments [54,55].

The bed expansion is compared with the results presented by Passalacqua et al. [31] using the Gidaspow drag model (Fig. 10),

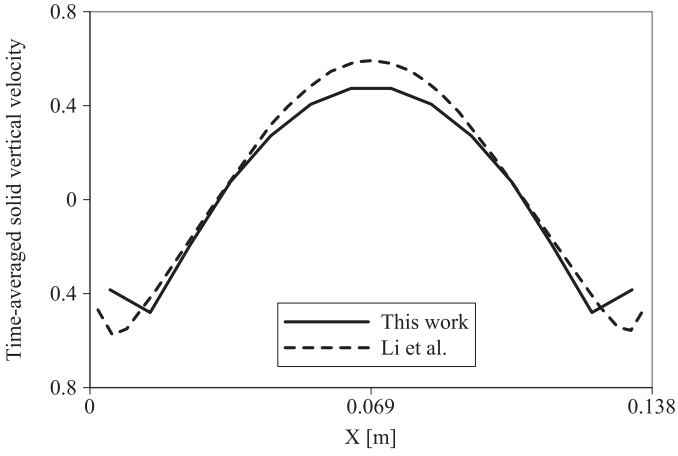

Fig. 9. Time-averaged solid vertical velocity profile at $y = 0.16$ m.

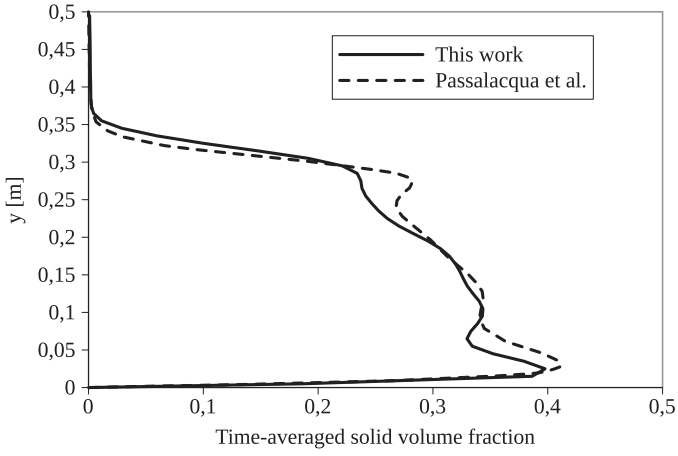

Fig. 10. Time-averaged solid volume fraction along a vertical center line compared with Passalacqua et al.

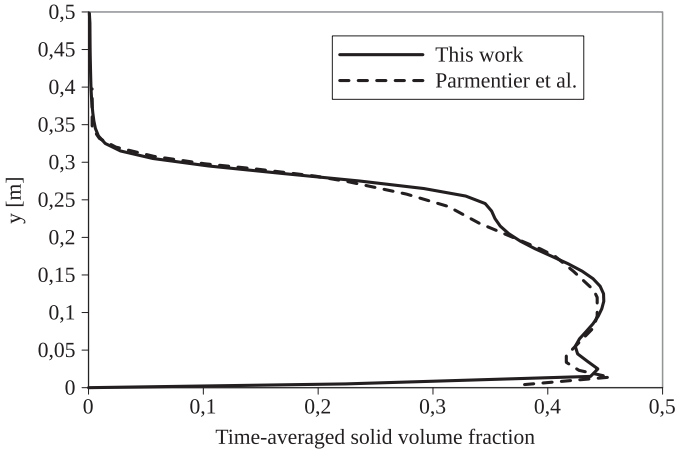

Fig. 11. Time and spatial-averaged solid volume fraction along a vertical line compared with Parmentier et al.

and with the results presented by Parmentier et al. [2] using the Wen–Yu drag model (Fig. 11). The results show a good agreement with the simulations done by the reference authors.

Fig. 12 shows the impact of the drag force models on the fluidized bed expansion. Here, the Gidaspow model predicts the highest expansion, followed by the Syamlal model and the Wen–Yu

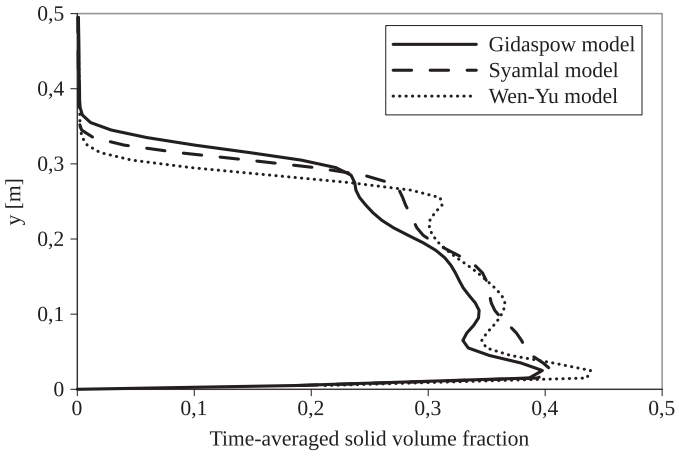

Fig. 12. Time-averaged solid volume fraction distribution for different drag models.

model, which is in agreement with the observations of Loha et al. [3].

5. Conservative analysis

In the previous section, the general performance of the solver was tested for two standard gas–particle problems and some numerical issues were addressed. The purpose of this section is to highlight the differences between the various levels of conservativeness of the advective term formulation on the momentum equations and its impact on the velocity field predictions.

5.1. One-dimensional approach

The finite volume method derives from the integral form of the conservative laws. Thus, in the spirit of obtaining a weak solution of the discrete problem, the use of a conservative method provides some degree of consistency in a mathematical sense. The *Lax–Wendroff theorem* proves that, if the approximation done by a conservative method converges to some function as the mesh is refined, then this function is a weak solution [32]. In fact, in problems where shock waves are involved, the use of a conservative method based on the integral form of the conservation laws, is essential to accurately predict the shock wave velocity. While no problems should arise for the calculation of smooth functions, nonconservative methods fail to converge to a weak solution when discontinuous functions are being transported. This behavior is illustrated by Leveque [32] for a one-dimensional transport of a step function using the Burgers equation. It is shown that the conservative method gives a wave velocity prediction in closer agreement to the analytical solution with respect to a nonconservative method. For a single time step, the difference in the predicted solution can be quantified as:

$$d_I = \left(u_k^{n+1}\right)_C - \left(u_k^{n+1}\right)_{NC} = \frac{1}{2}\Delta x\Delta t\left(\frac{u_k^n - u_{k-1}^n}{\Delta x}\right)^2 = \frac{1}{2}\Delta x\Delta t\,(u_x)^2 \tag{107}$$

where the subscript k is the cell index, n is the time step index, the subscript C correspond to the conservative formulation and the subscript NC to the nonconservative formulation. Also, the subscript x represents a discrete spatial derivative.

Here, upwind and forward-Euler schemes were employed for the spatial and temporal discretizations, respectively. It is clear that the differences in the velocity predictions become small for smooth solutions. Also, $d_I \geq 0$ which indicates that the nonconservative method always gives a smaller prediction of the shock wave velocity.

This conceptual problem clarifies the importance of using a conservative method to solve problems in presence of shock waves. However, the extension of these concepts to the momentum equations of the Eulerian multiphase model still deserves a discussion. For a conservative approach, Eq. (32) can be rewritten in the following form:

$$\frac{\partial}{\partial t}(\alpha_i \mathbf{u}_i) + \nabla\cdot(\alpha_i \mathbf{u}_i \mathbf{u}_i) = \mathbf{R}_i \tag{108}$$

where $\mathbf{R}_i$ represents all the terms on the right-hand-side of Eq. (32) (which do not play a relevant role in this analysis). It is recalled that ρ_i has been taken out of the derivative operators. This does not alter the conservative nature of the expression since ρ_i is always considered a constant for the purpose of this model.

It is a common practice to correct the momentum equations by subtracting the corresponding phase continuity equation. This is done to avoid errors in the solution of the momentum equation due to continuity imbalances [33,56].

Then, Eq. (108) becomes:

$$\frac{\partial}{\partial t}(\alpha_i \mathbf{u}_i) + \nabla\cdot(\alpha_i \mathbf{u}_i \mathbf{u}_i) - \mathbf{u}_i\frac{\partial \alpha_i}{\partial t} - \mathbf{u}_i\nabla\cdot(\alpha_i \mathbf{u}_i) = \mathbf{R}_i \tag{109}$$

Eq. (109) will be referred as the *conservative form* from now on. The second and fourth term is approximated using the finite volume method as:

$$\int_V \nabla\cdot(\alpha_i \mathbf{u}_i \mathbf{u}_i)dV - \int_V \mathbf{u}_i\nabla\cdot(\alpha_i \mathbf{u}_i)dV \approx \int_S \alpha_i \mathbf{u}_i \mathbf{u}_i\cdot\mathbf{dS} - \mathbf{u}_i\int_S \alpha_i \mathbf{u}_i\cdot\mathbf{dS} \approx \sum_f (\alpha_i \mathbf{u}_i)_f \varphi_i - \mathbf{u}_i\sum_f \alpha_{i,f}\varphi_i \tag{110}$$

and the following semi-discrete form is obtained:

$$\frac{\partial}{\partial t}(\alpha_i \mathbf{u}_i) - \mathbf{u}_i\frac{\partial \alpha_i}{\partial t} + \sum_f (\alpha_i \mathbf{u}_i)_f \varphi_i - \mathbf{u}_i\sum_f \alpha_{i,f}\varphi_i = \mathbf{R}_i \tag{111}$$

Here $\mathbf{u}_i$ and α_i have been indistinctly used to represent both continuous and cell-centered discrete variables. This is the formulation currently adopted in many commonly known multiphase solver codes [34,39,57]. This may be expressed in OpenFOAM code as:

```
fvVectorMatrix UEqn
(
    fvm::ddt(alpha, U)
  - fvc::Sp(fvc::ddt(alpha), U)
  + fvc::div(alphaf*phi, U)
  - fvc::Sp(fvc::div(alphaf*phi), U)
  - fvc::Sp(Rc)
);
```

Here `ddt` is the time-derivative operator, `Sp` is used to refer to the source or reactive terms and `div` is the divergence operator. The `Rc` term usually represents the diffusive, reactive and source terms in a Navier–Stokes problem, but here it is expressed as a single term for the sake of clarity. The advective terms are discretized explicitly (with the `fvc` operator) to simplify the subsequent

analysis. Also:

```
surfaceScalarField alpha1f = fvc::interpolate
(alpha1);
surfaceScalarField phi = linearInterpolate(U)
& mesh.Sf();
```

where the `interpolate` operator takes cell-centered values as inputs and returns an interpolated value in faces according to the interpolation scheme selected by the user. In OpenFOAM, the flux `phi` is implemented as a linear interpolation of the cell-centered velocities.

On the other hand, a nonconservative formulation may be obtained by operating with the second and fourth term of Eq. (109) which leads to the following form:

$$\frac{\partial}{\partial t}(\alpha_i \mathbf{u}_i) + \alpha_i \mathbf{u}_i \cdot \nabla \mathbf{u}_i - \mathbf{u}_i \frac{\partial \alpha_i}{\partial t} = \mathbf{R}_i \tag{112}$$

Eq. (112) will be referred as the *nonconservative form*. This form is somehow unnatural for numerical methods based on the integral form of the conservative laws since the *Gauss theorem* does not simplify the spatial derivative operators and it is unused in the available codes with few exceptions [58]. The semi-discrete form of Eq. (112) is obtained by considering:

$$\int_V \alpha_i \mathbf{u}_i \cdot \nabla \mathbf{u}_i dV \approx \alpha_i \mathbf{u}_i \cdot \int_V \nabla \mathbf{u}_i dV = \alpha_i \mathbf{u}_i \cdot \int_S \mathbf{u}_i \mathbf{dS} \approx \alpha_i \mathbf{u}_i \cdot \sum_f \mathbf{Su}_{i,f} \tag{113}$$

thus arriving to

$$\frac{\partial}{\partial t}(\alpha_i \mathbf{u}_i) - \mathbf{u}_i \frac{\partial \alpha_i}{\partial t} + \alpha_i \mathbf{u}_i \cdot \sum_f \mathbf{Su}_{i,f} = \mathbf{R}_i \tag{114}$$

In OpenFOAM code this becomes:

```
fvVectorMatrix UEqn
  (
    fvm::ddt(alpha, U)
    - fvc::Sp(fvc::ddt(alpha), U)
    + fvc::div(alphaf*phi, U)
    - fvc::Sp(fvc::div(alphaf*phi), U)
    - fvc::Sp(Rc)
  );
```

Park [33] showed the differences of using both formulations (Eqs. (111) and (114)) in a few test cases, and emphasized on the importance of using a formulation as conservative as possible to accurately predict the velocity field. This analysis is resumed in this work with the incorporation of a different nonconservative formulation: the *phase-intensive form* [29,30]. This formulation can be obtained by rewriting the scalar product on the second term of Eq. (112):

$$\frac{\partial}{\partial t}(\alpha_i \mathbf{u}_i) + \alpha_i \nabla \cdot (\mathbf{u}_i \mathbf{u}_i) - \alpha_i \mathbf{u}_i (\nabla \cdot \mathbf{u}_i) - \mathbf{u}_i \frac{\partial \alpha_i}{\partial t} = \mathbf{R}_i \tag{115}$$

The semi-discrete version of this formulation is obtained by rewriting the second and third term on Eq. (115) as:

$$\int_V \alpha_i \nabla \cdot (\mathbf{u}_i \mathbf{u}_i) dV - \int_V \alpha_i \mathbf{u}_i (\nabla \cdot \mathbf{u}_i) dV \approx \alpha_i \int_S \mathbf{u}_i \mathbf{u}_i \cdot \mathbf{dS} - \alpha_i \mathbf{u}_i \int_S \mathbf{u}_i \cdot \mathbf{dS} \approx \alpha_i \sum_f \mathbf{u}_{i,f} \varphi_i - \alpha_i \mathbf{u}_i \sum_f \varphi_i \tag{116}$$

and finally

$$\frac{\partial}{\partial t}(\alpha_i \mathbf{u}_i) - \mathbf{u}_i \frac{\partial \alpha_i}{\partial t} + \alpha_i \sum_f \mathbf{u}_{i,f} \varphi_i - \alpha_i \mathbf{u}_i \sum_f \varphi_i = \mathbf{R}_i \tag{117}$$

which may be written in OpenFOAM code as:

```
fvVectorMatrix UEqn
  (
    fvm::ddt(alpha, U)
    - fvc::Sp(fvc::ddt(alpha), U)
    + ((alpha*U) & fvc::grad(U))
    - fvc::Sp(Rc)
  );
```

The analysis done by Leveque for the Burgers equation may be extended to the Eulerian two-phase momentum equations for one-dimensional problems. A fully discrete version of the *conservative form* is obtained using an upwind method for the face interpolations (with the exception of the flux φ which is always linearly interpolated) and a forward-Euler for the temporal derivatives. Then, Eq. (111) becomes:

$$\frac{V}{\Delta t}\alpha_k^n (u_k^{n+1} - u_k^n) - \frac{V}{\Delta t} u_k^n (\alpha_k^n - \alpha_k^{n-1}) + (\alpha^n u^n)_{k+\frac{1}{2}} \varphi_{k+\frac{1}{2}}^n + (\alpha^n u^n)_{k-\frac{1}{2}} \varphi_{k-\frac{1}{2}}^n - u_k^n \alpha_{k+\frac{1}{2}}^n \varphi_{k+\frac{1}{2}}^n - u_k^n \alpha_{k-\frac{1}{2}}^n \varphi_{k-\frac{1}{2}}^n = R_k^n V \tag{118}$$

where the fractional index represents face interpolations of the cell-centered values. Thus:

$$\alpha_k^n (u_k^{n+1} - u_k^n)\left(\frac{V}{\Delta t}\right) - u_k^n (\alpha_k^n - \alpha_k^{n-1})\left(\frac{V}{\Delta t}\right) + \alpha_k^n u_k^n \left(\frac{u_{k+1}^n + u_k^n}{2}\right)\left(\frac{V}{\Delta x}\right) + \alpha_{k-1}^n u_{k-1}^n \left(\frac{u_k^n + u_{k-1}^n}{2}\right)\left(\frac{V}{\Delta x}\right) - \alpha_k^n u_k^n \left(\frac{u_{k+1}^n + u_k^n}{2}\right)\left(\frac{V}{\Delta x}\right) - \alpha_{k-1}^n u_k^n \left(\frac{u_k^n + u_{k-1}^n}{2}\right) \times \left(\frac{V}{\Delta x}\right) = R_k^n V \tag{119}$$

This leads to an expression for the predicted velocity at the next time step given by:

$$\left(u_k^{n+1}\right)_C = u_k^n \left(2 - \frac{\alpha_k^{n-1}}{\alpha_k^n}\right) + \frac{\Delta t}{\Delta x}\frac{1}{\alpha_k^n} R_k^n - \frac{\Delta t}{\Delta x}\frac{\alpha_{k-1}^n}{2\alpha_k^n}\left[\left(u_k^n\right)^2 - \left(u_{k-1}^n\right)^2\right] \tag{120}$$

The same procedure may be performed for the nonconservative formulations (Eqs. (114) and (117)), leading to:

$$\left(u_k^{n+1}\right)_{NC} = u_k^n \left(2 - \frac{\alpha_k^{n-1}}{\alpha_k^n}\right) + \frac{\Delta t}{\Delta x}\frac{1}{\alpha_k^n} R_k^n - \frac{\Delta t}{\Delta x} u_k^n \left(u_k^n - u_{k-1}^n\right) \tag{121}$$

$$\left(u_k^{n+1}\right)_{PI} = u_k^n \left(2 - \frac{\alpha_k^{n-1}}{\alpha_k^n}\right) + \frac{\Delta t}{\Delta x}\frac{1}{\alpha_k^n} R_k^n - \frac{\Delta t}{\Delta x}\frac{1}{2}\left[\left(u_k^n\right)^2 - \left(u_{k-1}^n\right)^2\right] \tag{122}$$

where the subscript C correspond to the *conservative form*, the subscript NC to the *nonconservative form* and the subscript PI to the *phase-intensive form*. The phase index has been omitted for simplicity. The reader may notice that Eqs. (120)–(122) are equal but for the last term. Therefore, any difference between the velocity predictions would be related to this term.

In order to illustrate the relative accuracy of the three methods, a one-dimensional dam break problem is considered. Here, the shallow water equations are used to predict the velocity u and water level α (which plays a similar role to the volume fraction in the two-phase model):

$$\frac{\partial \alpha}{\partial t} + \frac{\partial}{\partial x}(\alpha u) = 0 \tag{123}$$

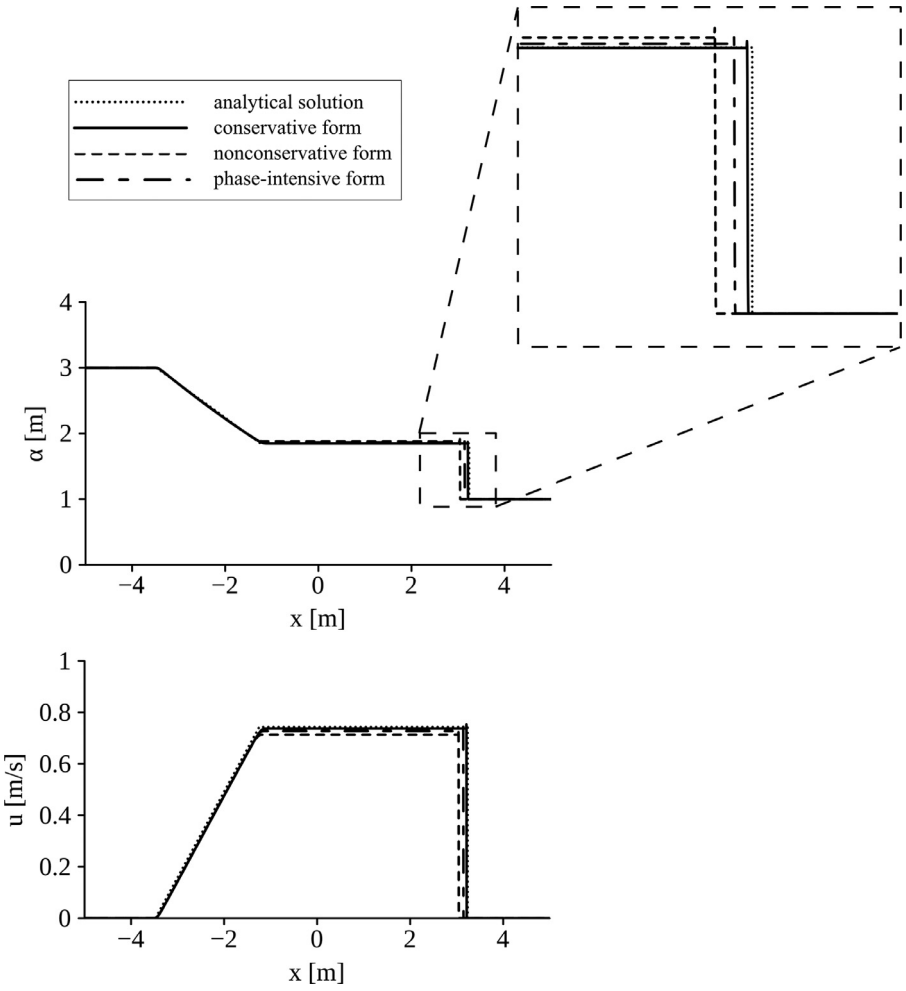

Fig. 13. Liquid level and velocity at $t = 2$ s for different formulations.

$$\frac{\partial}{\partial t}(\alpha u) + \frac{\partial}{\partial x}(\alpha u^2) + \frac{\partial}{\partial x}\left(\frac{1}{2} g \alpha^2\right) = 0 \tag{124}$$

with the following initial conditions:

$$u = 0,\ x \in (-5; 5)$$
$$\alpha = \begin{cases} 3,\ x \in (-5; 0) \\ 1,\ x \in [0; 5) \end{cases} \tag{125}$$

While this model is much simpler than the two-dimensional multiphase Eulerian model, it is possible to obtain an analytical solution to compare with the numerical predictions. This may be done through an eigenvalue analysis, which leads to an expression for the shock wave velocity given by $s = u + g\alpha$ [32]. The solution at a given time for different advective formulations is shown in Fig. 13, where a rarefaction wave travels to the left and a shock wave travels to the right. For smooth variations of the transported fields (at the rarefaction wave), no difference is appreciated between formulations. But, at the shock wave, the *conservative form* clearly gives a higher and more accurate wave velocity prediction.

The differences on the numerical solutions among the various levels of conservativeness considered in a single time step can be quantified by subtracting Eqs. (120)–(122) with each other:

$$d_{C-PI} = \frac{1}{2}\Delta x \Delta t \left(\frac{1}{\alpha_k^n}\right)\left[\frac{\left(u_k^n\right)^2 - \left(u_{k-1}^n\right)^2}{\Delta x}\right]\left(\frac{\alpha_k^n - \alpha_{k-1}^n}{\Delta x}\right)$$
$$= \frac{1}{2}\Delta x \Delta t \left(\frac{1}{\alpha}\right)\alpha_x \left(u^2\right)_x \tag{126}$$

$$d_{PI-NC} = \frac{1}{2}\Delta x \Delta t \left(\frac{u_k^n - u_{k-1}^n}{\Delta x}\right)^2 = \frac{1}{2}\Delta x \Delta t\ (u_x)^2 \tag{127}$$

$$d_{C-NC} = d_{C-PI} + d_{PI-NC} = \frac{1}{2}\Delta x \Delta t \left[\left(\frac{1}{\alpha}\right)\alpha_x \left(u^2\right)_x + (u_x)^2\right] \tag{128}$$

There are several observations to be made about these expressions. In all cases, these differences increase when there are discontinuities in u and α. The reader may notice that Eq. (127) is equal to Eq. (107). This is expected since the advective terms for the two-phase model and the Burgers equation are the same, except for the presence of α_i. However, as it is clear from Eq. (127), this field does not have an impact on the differences between the velocity predictions of the *phase-intensive form* and the *nonconservative form*. Also, this expression is always positive when the velocity field varies, which means that, for a one-dimensional problem, the *phase-intensive form* always predicts a higher wave velocity than the *nonconservative form*. The analysis of Eqs. (126) and (128) is not as straightforward. The differences of both nonconservative formulations with respect to the *conservative form* have the influence of the volume fraction field variation. Therefore, these expressions may take both positive and negative signs depending on the relative "jumps" of α and u fields.

The *phase-intensive form* has been largely adopted in two-phase solvers as a robust way of dealing with the phase disappearance in the momentum equations, but little is said about its accuracy with respect to a conservative formulation. Park et al. [33] analyzed the differences between the *conservative form* and *nonconservative form*

with practical examples. However, as shown in Eq. (127), the differences between the *phase-intensive form* and *nonconservative form* may be significant. In fact, depending on the studied case, the *phase-intensive form* may predict closer results to the *conservative form* than the *nonconservative form* (as shown in the previous example). In general:

$$\alpha_x(u^2)_x \geq 0 \Rightarrow |d_{C-NC}| \geq |d_{C-PI}| \tag{129}$$

which means that, with respect to the *conservative form* velocity solution, the *phase-intensive form* will predict a more accurate result than the *nonconservative form*. However, this is not guaranteed when α and u^2 have opposite variations. In these conditions, small values of α_x with respect to u_x will favor the accuracy of the *phase-intensive form* since:

$$\lim_{\alpha_x \to 0} |d_{C-PI}| = 0 \tag{130}$$

and

$$\lim_{\alpha_x \to 0} |d_{C-NC}| = |d_{PI-NC}| \tag{131}$$

5.2. Phase disappearance treatment

The limit where α_s tends to zero is an issue that is closely related to the momentum equations handling since, in this condition, the equations in its *conservative form* become singular. This translates into an impediment for the iterative procedure to converge to a prescribed tolerance.

This problem may be avoided by setting the disperse phase velocity equal to the velocity of the continuous phase in those cells where the particles phase fraction gets below a certain critical value. A natural way to achieve this is to preserve the drag force as a non-zero term in the momentum equations when α_s tends to zero. Thus, the phase momentum equation is reduced to:

$$\frac{K_{sg}}{\rho_s}(\mathbf{u}_g - \mathbf{u}_s) = 0 \tag{132}$$

If $K_{sg} \neq 0$, then $\mathbf{u}_s = \mathbf{u}_g$, which may be guaranteed by computing the drag coefficient (for example using the Wen–Yu model) as:

$$K_{sg} = 0.75\frac{C_d \alpha_{s,\text{low}} \alpha_g^{-1.65} \rho_g}{d_p}\max(|\mathbf{u}_g - \mathbf{u}_s|, \mathrm{U}_{r,\text{low}}) \tag{133}$$

where $\alpha_{s,\text{low}}$ and $\mathrm{U}_{r,\text{low}}$ are some minimal residual values to avoid singular expressions. This method is currently implemented in OpenFOAM® [34]. While this method may be considered physically correct (the disperse phase velocity tending to the continuous phase velocity as the disperse phase tends to disappear) it has its drawbacks. For example, in a fluidized bed problem, the particles are carried out of the domain when $\alpha_s \leq \alpha_{s,\text{low}}$. In this condition, the solid phase takes the velocity of the gas phase, which would be correct when $\alpha_s \to 0$.

An alternative to avoid a singular momentum matrix without the previous issue is to compute $\mathbf{u}_s$ from a force balance between the drag, buoyancy, particle pressure and shared pressure forces. Thus, the particles momentum equation may be written as:

$$0 = -\frac{\alpha_{s,\text{low}}}{\rho_s}\nabla p - \frac{1}{\rho_s}\nabla p_s(\alpha_{s,\text{low}}) + \alpha_{s,\text{low}}\mathbf{g} + \frac{K_{sg}(\alpha_{s,\text{low}})}{\rho_s}(\mathbf{u}_g - \mathbf{u}_s) labeleq : 5.28 \tag{134}$$

This method is somehow intrusive since all the remaining terms of the momentum equation are being modified from its correct continuum form. The *phase-intensive form* gets a relative advantage in this issue by following the procedure proposed by Oliveira et al. [29]. The reader may notice that the first two terms on Eqs. (111), (114) and (117) can be rewritten as:

$$\frac{\partial}{\partial t}(\alpha_i \mathbf{u}_i) - \mathbf{u}_i \frac{\partial \alpha_i}{\partial t} = \alpha_i \frac{\partial \mathbf{u}_i}{\partial t} \tag{135}$$

This allows a subsequent division by α_s in all terms of Eq. (112). Thus, the procedure isolates the singularity in the solid stress tensor term, which becomes proportional to $\nabla\alpha_s/\alpha_s$ and can be easily handled by numerical manipulation.

In this work, in order to maintain the same conditions for comparison between the different advective term treatments, a common criterion is adopted. The phase disappearing limit is addressed by setting the phase velocity to zero when the volume fraction gets below certain critical value. This should not be seen as an ideal solution but as a way to isolate the interest of the current study. Moreover, while the different transient term formulations also contribute to differences among the numerical predictions, the transient terms will be formulated as presented in the

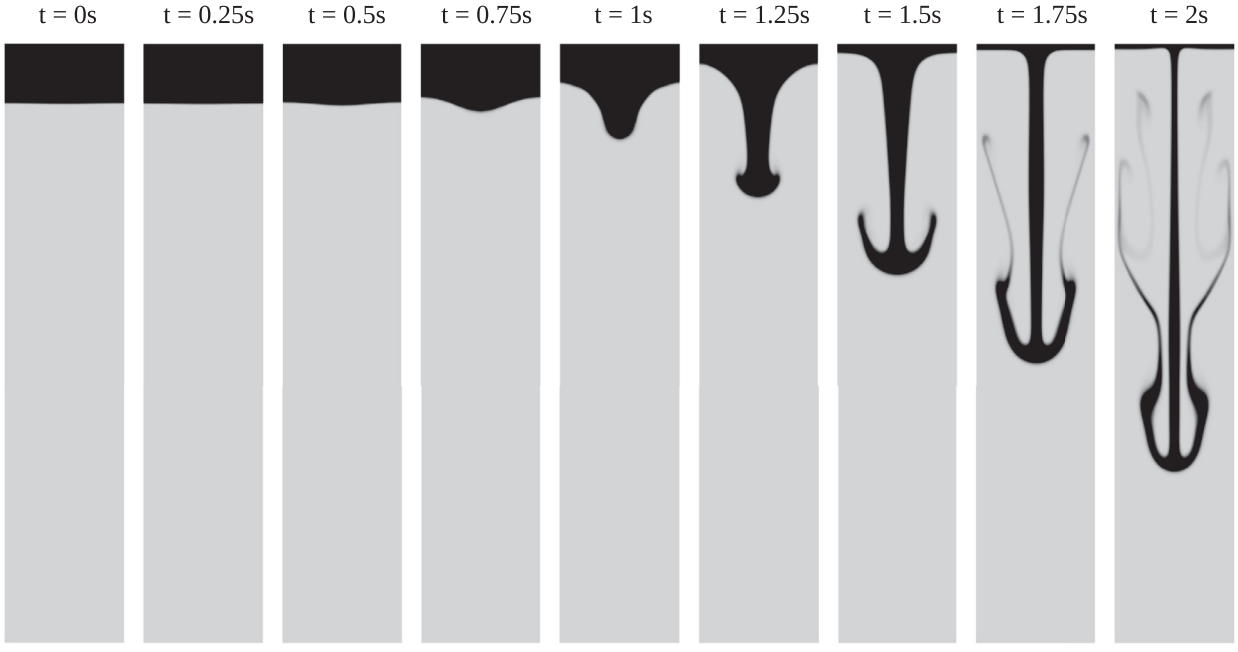

Fig. 14. Transient evolution of the Rayleigh–Taylor problem.

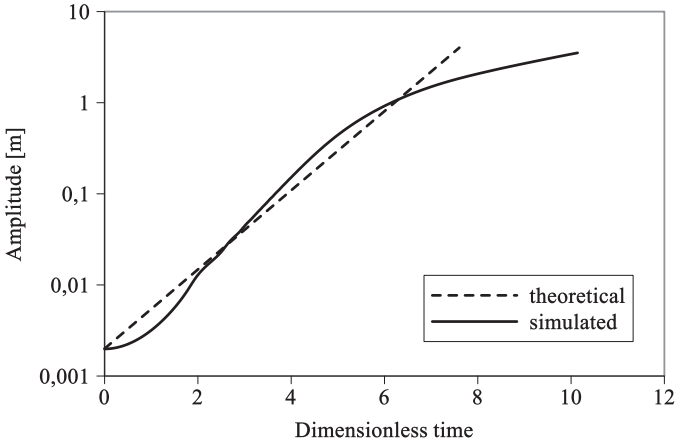

Fig. 15. Amplitude growth simulated against the linear prediction.

left-hand-side of Eq. (135). This is done to isolate the effect of the spacial term conservativeness.

5.3. Test cases

The exact difference in the velocity prediction of each formulation has been established and quantified for a given discretization on a one-dimensional problem. The following test cases are presented to illustrate how the differences appear on two-dimensional problems, where the shock waves are transported in multiple directions. The same conclusions can be extended to this problems by considering that the discrete system for the phase momentum balance may be expressed as:

$$\mathbf{A}\begin{pmatrix}\underline{u}\\ \underline{v}\end{pmatrix}^{n+1} = \mathbf{B}_{\{C,NC,PI\}}\begin{pmatrix}\underline{u}\\ \underline{v}\end{pmatrix}^{n} + \begin{pmatrix}\underline{r_u}\\ \underline{r_v}\end{pmatrix} \tag{136}$$

where **A** and **B** are the discretization matrices, $\underline{u}$ and $\underline{v}$ are the velocity vectors containing the cell values of the horizontal and vertical component respectively and $\underline{r_u}$ and $\underline{r_v}$ contain the source terms for each component. Following the same explicit discretization in time as for the one-dimensional case, different velocity predictions $\underline{u}^{n+1}$ and $\underline{v}^{n+1}$ are expected due to the matrix of coefficients **B** resulting of the different discretization procedures given by Eqs. (111), (114) and (117).

Unlike the one-dimensional dam-break problem, no analytical solutions are available for the following examples. Nonetheless, there are still features (i.e. mesh convergence analysis and experimental data) that may be looked into in order to determine the accuracy of each formulation.

5.3.1. Rayleigh–Taylor instability problem

A Rayleigh–Taylor instability problem is addressed using the Eulerian two-phase model. The problem consists of two fluid phases initially segregated in a vertical enclosure. The dense phase is purely concentrated in the upper region as depicted in Fig. 14. An initial disturbance on the interphase (described by Eq. (137)) is amplified by the effect of gravity forming a mushroom shape. The physical parameters of the problem are $\rho_s = 10.0\text{kg/m}^3$, $\rho_g = 1.0\text{kg/m}^3$, $\nu_s = \nu_g = 0.01\text{m/s}^2$ and the domain is a rectangular container of 1m × 5m.

$$\delta_0 = -0.001\left[\cos\left(\frac{2\pi x}{L} - \pi\right) + 1\right] + 4.5 \tag{137}$$

Different mesh refinements have been considered for this problem: 32 × 160 (4×), 64 × 320 (2×), 128 × 640 (1×), 256 × 1280 (1/2×) and 512 × 2560 (1/4×).

The initial growth of the interphase amplitude at the initial stage [59] is given by:

$$\delta = \delta_0 \cosh(\gamma t) \tag{138}$$

where $\gamma = \sqrt{\mathcal{A}g\lambda}$, $\mathcal{A} = \dfrac{\rho_s - \rho_g}{\rho_s + \rho_g}$ is the Atwood number and λ is the wave number.

During the linear evolution stage, a good level of agreement is found between simulation and theoretical predictions for the 1× mesh (Fig. 15).

The comparison between the conservative and nonconservative formulations is performed using upwind interpolations and an

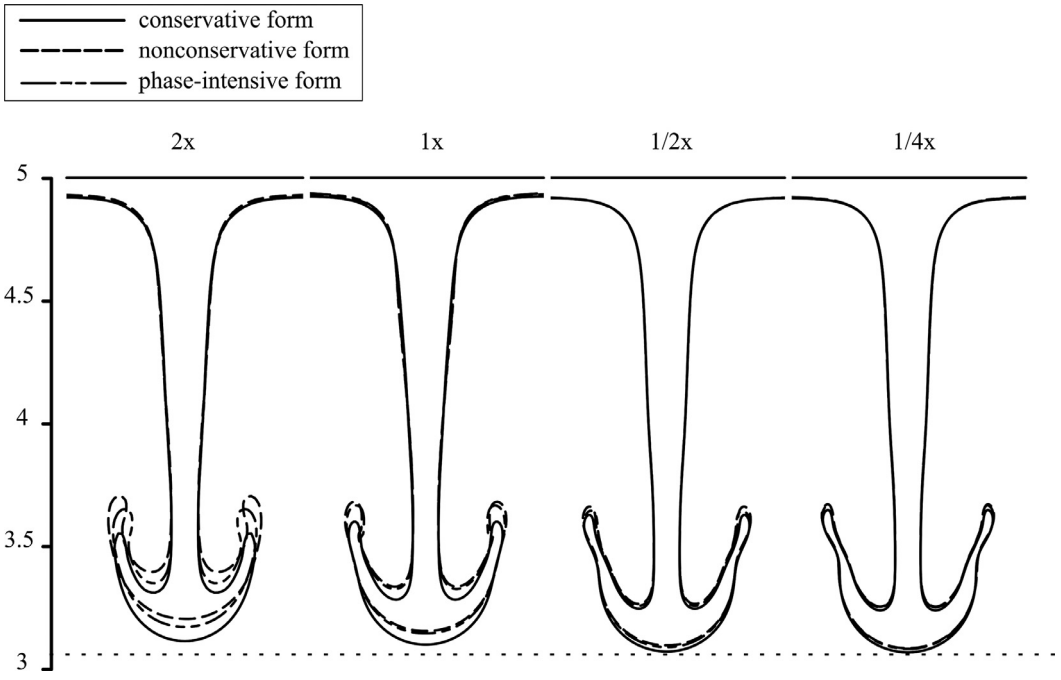

Fig. 16. Contour plots ($\alpha_g = 0.5$) with different mesh refinements and formulations at $t = 1.5$ s.

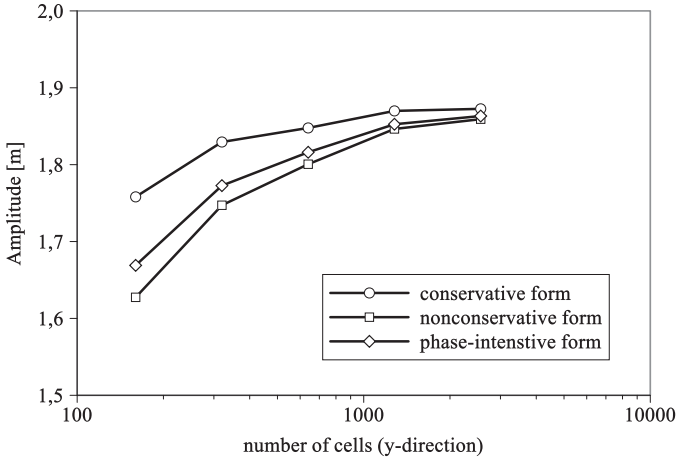

Fig. 17. Mushroom amplitude for different formulations and mesh refinements.

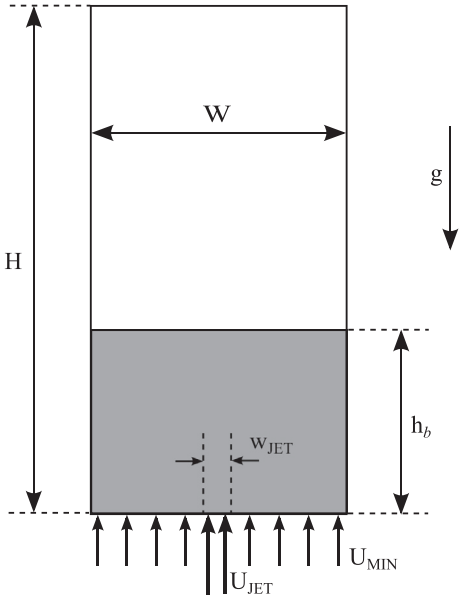

Fig. 18. Single bubble growth problem scheme.

explicit treatment of the advective terms. The solution tends to differ at the latter stages of the mushroom formation, where no theoretical solution is available. Nevertheless, the accuracy of each formulation can be studied through a mesh convergence analysis.

Table 2
Physical models and parameters.

Parameter	Value
Gas density	1.2 kg/m^3
Gas viscosity	1.84×10^{-5} Pa s
Solid density	2660 kg/m^3
Particles diameter	500×10^{-6} m
Restitution coefficient	0.95
Width (W)	0.57 m
Height (H)	1.0 m
Initial bed height (h_b)	0.5 m
Jet gap width (w_{JET})	0.015 m
Grid	152 × 200 cells
Time step	1.0×10^{-4} s
Drag model	Gidaspow
Frictional stress model	Srivastava and Sunderasan
Packing limit	0.65
Minimal frictional value	0.63
Jet inlet velocity (U_{JET})	10.0 m/s
Fluidization velocity (U_{MIN})	0.25 m/s
Initial bed solid fraction	0.598

Fig. 16 shows the interphase shape for different mesh refinements and formulations at $t = 1.5$ s.

It is clear from Fig. 17 that all formulations tend to the same solution as the mesh is refined, but the *conservative form* always predicts the fastest growth of the interphase and has closer agreement with the mesh converged solution. Moreover, the *conservative form* for a coarse mesh of 1× predicts an amplitude similar to the predictions of the nonconservative formulations with the finest mesh (1/4×). Therefore, the adoption of the *conservative form* could be used to minimize the computational costs involved in predicting the amplitude evolution for a given accuracy.

5.3.2. Single bubble growth

A two-dimensional single air bubble growth and detachment in a particles fluidized bed is now considered. This problem consists of an air injection at the bottom of a cylindrical container partially filled with particles at a state of minimum fluidization (Fig. 18).

The geometry and general setup of the problem are based on the experiment performed by Kuipers et al. [60] and are summarized in Table 2.

Patil et al. [9] showed the need to take into account the frictional contribution to compute the global stress tensor in order to accurately predict the bubble size and bed expansion. Moreover, Passalacqua et al. [61] showed that commonly used frictional models fail to correctly predict the bubble diameter, while a modified Srivastava–Sunderasan model (with $\alpha_{s,min} = 0.63$ and $\alpha_{s,max} = 0.65$) exhibits closer agreement with the experimental results.

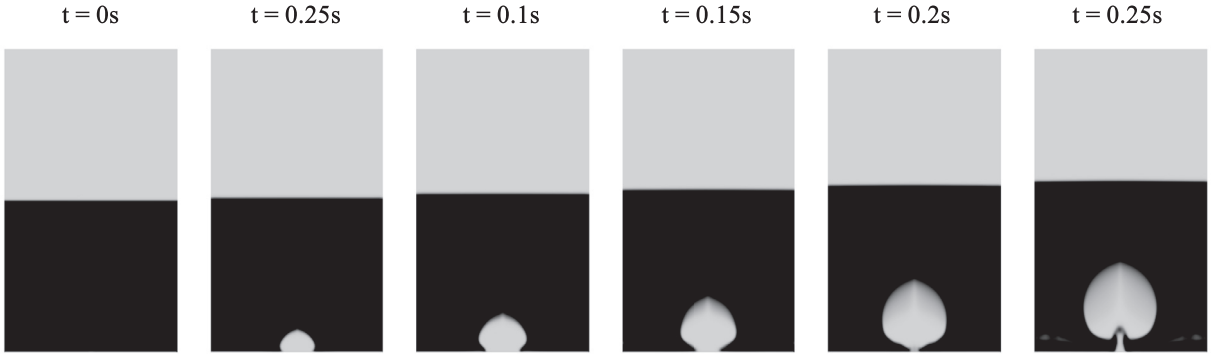

Fig. 19. Transient evolution of a single bubble growth problem.

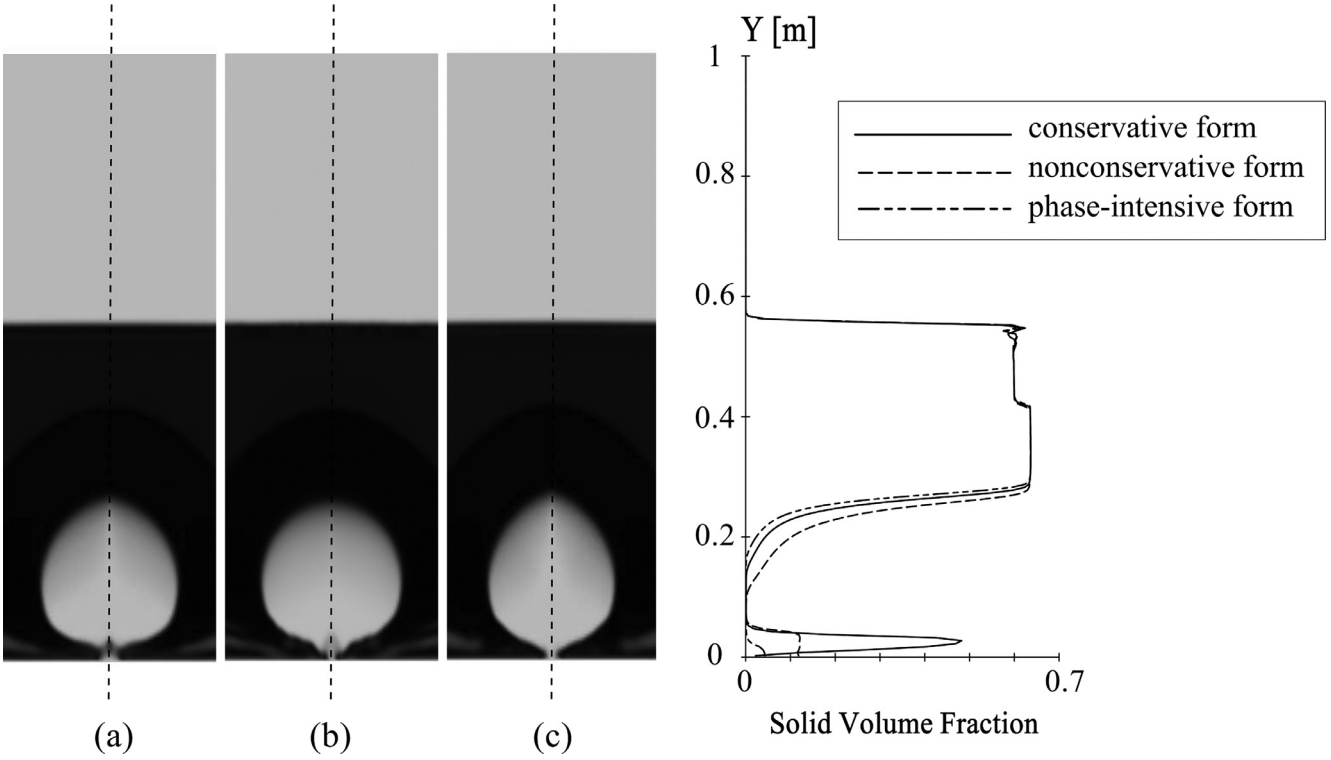

Fig. 20. Bubble shapes at $t = 0.22$ s for (a) the *conservative form*, (b) the *nonconservative form* and (c) the *phase-intensive form*

Table 3
Detachment time for different mesh refinements and different formulations.

Exp		0.170 s	
Mesh refinement	C	NC	PI
1/2 × (304 × 400 cells)	0.176 s	–	0.201 s
1× (152 × 200 cells)	0.182 s	0.182 s	0.205 s
2× (76 × 100 cells)	0.180 s	0.196 s	0.194 s
4× (38 × 50 cells)	0.182 s	0.200 s	0.198 s

This test case introduces the complexity of the particles interaction to the conservative method analysis. The transient evolution of the air bubble until the detachment from the bottom is shown in Fig 19.

Fig. 20 shows differences between formulations in terms of the bubble shape and detachment time. It is appreciated that the *phase-intensive form* predicts a more stretched and pointy bubble while the *nonconservative form* predicts a more round bubble. The *conservative form* predicts a shape that is in between these two. Moreover, several mesh refinements were tested and, from Table 3, it is appreciated that the *conservative form* predicts the lowest detachment time with the closest agreement with the experimental data reported in the literature [60].

5.3.3. Fluidized bed

The bubbling fluidized bed problem studied in the previous section is now tested using the *conservative form* and the *phase-intensive form*. Figs. 21–23 show time-averaged particles distribution and vertical velocity for both formulations. Slight differences in the particles concentration are observed in the upper region of the bed. However, the differences are minimal in the mid region, and the predicted bed expansion with both formulations are in agreement. Also, the results for both formulations of the averaged particles velocity and volume fraction in the cross-axial direction are in an acceptable agreement.

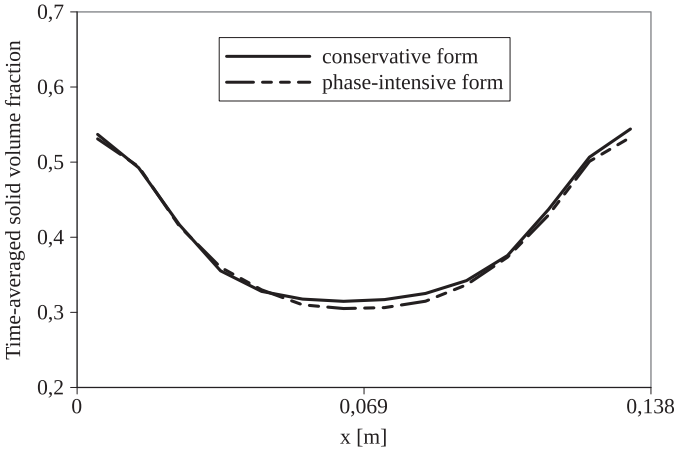

Fig. 21. Averaged solid volume fraction at $y = 0.16$ m for different formulations.

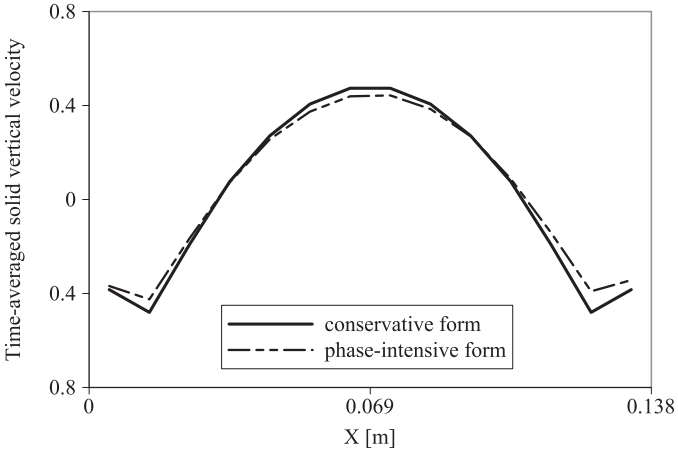

Fig. 22. Averaged solid vertical velocity at $y = 0.16$ m for different formulations.

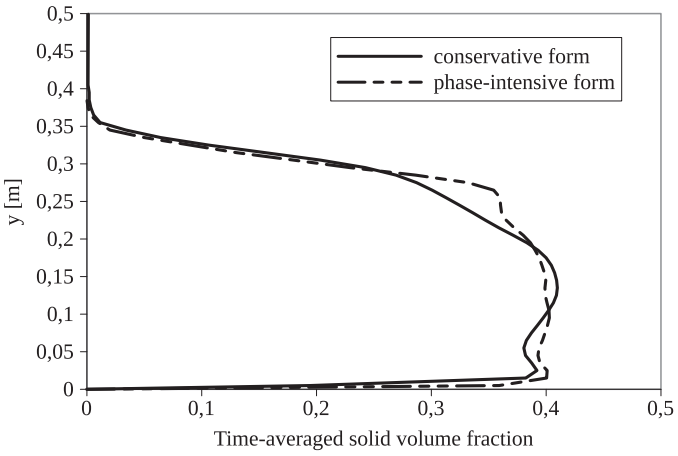

Fig. 23. Averaged solid volume fraction along the bed height for different formulations.

Unlike the previous test cases, in this problem, the bubbles formation, growth and coalescence induce velocity waves that travel in multiple directions. Due to this, the time averaging practice tends to mitigate any substantial difference between the predictions of the advective term formulations.

6. Conclusions

An Eulerian multiphase finite volume-based solver was developed and implemented on the OpenFOAM® platform. The solver was tested exhaustively against a particles settling and a two-dimensional fluidized bed problem. Its numerical performance was explored under demanding conditions such as single-phase and maximum packing limits, shock wave transport, among others. Also, in the fluidized bed problem, various models of the drag coefficient were used for which the averaged solutions have a recognized sensitivity. In all cases, the results were stable during the transient states and with close agreement with the literature.

The open-source feature of the code has allowed to implement and test the performance for different drag coupling methods. The results showed that the PEA and PIM have a satisfactory performance for moderate coupling conditions. However, the use of the PEA becomes essential for the solution of highly coupled flows, commonly observed in pneumatic transport problems, bubbling fluidized bed with Geldart A particles, among others.

A conservative analysis of the advective term of the momentum equations was also performed. Three different formulations were tested in problems with discontinuities on the velocity field. A one-dimensional analysis was addressed and the exact difference between the velocity predictions was quantified for a single time step. It was found that the *phase-intensive form* always predicts a higher shock wave velocity than the *nonconservative form* and the difference with the *conservative form* prediction depends on the relative variations of α and u. The conditions at which these differences minimize were also discussed. Then, the analysis was extended to a series of two-dimensional problems. First, a Rayleigh–Taylor instability problem was considered. Here, a mesh convergence analysis was performed to evaluate the development of the mushroom shape formed by the interphase. It was found that, for coarse meshes, the *conservative form* gives closer results to the mesh converged solution. Next, a bubble growth in a particulate fluidized bed problem was addressed. Results show that the *phase-intensive form* predicts a more stretched bubble while the *non-conservative form* predicts a flatter and wider bubble. The *conservative form* falls in between those shapes, but with a time of detachment lower than the other formulations. This is in agreement with the experimental results of the literature. Finally, the *conservative form* and *phase-intensive form* were compared in a bubbling fluidized bed problem. It was shown that the effects of these formulations have a low impact on macroscopic results, such as the time-averaged particles distribution. The analysis of these problems showed that:

- The *conservative form* adoption is essential for unsteady problems with presence of shock waves (which are commonly found in many multiphase applications). The implementation of this formulation has to be done along with a proper handling of the phase disappearance condition.
- The *nonconservative form* is not recommended for multiphase applications since the predicted velocity field is usually far from the real solution.
- The *phase-intensive form* fails to accurately predict the velocity fields for detailed unsteady conditions when shock waves are present, but, for the analysis of averaged particles distributions, it gets a satisfactory performance in comparison with the conservative formulation. Added to this, the issues related to the phase disappearance are easily handled with this formulation.

Acknowledgment

The authors wish to thank CONICET, Universidad Nacional del Litoral and ANPCyT for their financial support through grants CAI+D 2011 501 201101 00435 LI and PICT-2013 0830. Part of the computing was done in Coyote cluster which was funded by CONICET (grants PIP 0341, 2009 and PIP 2956, 2009) and ANPCyT (Grant PICT 2492, 2010)

References

[1] Min J, Drake JB, Heindel TJ, Fox RO. Experimental validation of CFD simulations of a lab-scale fluidized-bed reactor with and without side-gas injection. AIChE J 2010;56(6):1434–46.
[2] Parmentier J-F, Simonin O, Delsart O. A numerical study of fluidization behavior of Geldart B, A/B and A particles using an Eulerian multifluid modeling approach. In: Proceedings of the IX circulating fluidized bed technology conference, Hamburg, Germany; 2008.
[3] Loha C, Chattopadhyay H, Chatterjee PK. Assessment of drag models in simulating bubbling fluidized bed hydrodynamics. Chem Eng Sci 2012;75:400–7.
[4] Makkawi YT, Wright PC, Ocone R. The effect of friction and inter-particle cohesive forces on the hydrodynamics of gas–solid flow: a comparative analysis of theoretical predictions and experiments. Powder Technol 2006;163(1):69–79.
[5] Almuttahar A, Taghipour F. Computational fluid dynamics of a circulating fluidized bed under various fluidization conditions. Chem Eng Sci 2008;63(6):1696–709.
[6] Ding J, Gidaspow D. A bubbling fluidization model using kinetic theory of granular flow. AIChE J 1990;36(4):523–38.
[7] Huilin L, Gidaspow D, Bouillard J, Wentie L. Hydrodynamic simulation of gas–solid flow in a riser using kinetic theory of granular flow. Chem Eng J 2003;95(1):1–13.
[8] Taghipour F, Ellis N, Wong C. Experimental and computational study of gas—solid fluidized bed hydrodynamics. Chem Eng Sci 2005;60(24):6857–67.
[9] Patil D, van Sint Annaland M, Kuipers J. Critical comparison of hydrodynamic models for gas–solid fluidized beds - Part I: Bubbling gas–solid fluidized beds operated with a jet. Chem Eng Sci 2005a;60(1):57–72.
[10] Patil D, van Sint Annaland M, Kuipers J. Critical comparison of hydrodynamic models for gas–solid fluidized beds - Part II: Freely bubbling gas–solid fluidized beds. Chem Eng Sci 2005b;60(1):73–84.
[11] Ishii M. Thermo-fluid dynamic theory of two-phase flow. NASA STI/Recon Tech Rep A 1975;75:29657.
[12] Drew DA. Continuum modeling of two-phase flows. Technical Report. DTIC Document. DTIC; 1982.
[13] Bagnold RA. Experiments on a gravity-free dispersion of large solid spheres in a Newtonian fluid under shear. Proc R Soc Lond A: Math Phys Eng Sci 1954;225:49–63.
[14] Lun C, Savage S, Jeffrey D, Chepurniy N. Kinetic theories for granular flow: inelastic particles in Couette flow and slightly inelastic particles in a general flowfield. J Fluid Mech 1984;140:223–56.
[15] Gidaspow D. Multiphase flow and fluidization: continuum and kinetic theory descriptions. Academic Press; 1994.
[16] Chapman S, Cowling TG. The mathematical theory of non-uniform gases: an account of the kinetic theory of viscosity, thermal conduction and diffusion in gases. Cambridge University Press; 1970.

[17] Lyczkowski RW, Gamwo IK, Dobran F, Ai Y, Chao B, Chen M, et al. Validation of computed solids hydrodynamics and pressure oscillations in a bubbling atmospheric fluidized bed. Powder Technol 1993;76(1):65–77.
[18] Bouillard J, Lyczkowski R, Gidaspow D. Porosity distributions in a fluidized bed with an immersed obstacle. AIChE J 1989;35(6):908–22.
[19] Schaeffer DG. Instability in the evolution equations describing incompressible granular flow. J Differ Equ 1987;66(1):19–50.
[20] Johnson PC, Jackson R. Frictional–collisional constitutive relations for granular materials, with application to plane shearing. J Fluid Mech 1987;176:67–93.
[21] Srivastava A, Sundaresan S. Analysis of a frictional–kinetic model for gas–particle flow. Powder Technol 2003;129(1):72–85.
[22] Ergun S. Fluid flow through packed columns. Chem Eng Prog 1952;48:89–94.
[23] Wen C, Yu Y. Mechanics of fluidization. Chem Eng Prog Symp 1966;62:100–11.
[24] Syamlal M. The particle-particle drag term in a multiparticle model of fluidization. Technical Report. Morgantown, WV, USA: EG and G Washington Analytical Services Center, Inc.; 1987.
[25] Gibilaro L, Di Felice R, Waldram S, Foscolo P. Generalized friction factor and drag coefficient correlations for fluid–particle interactions. Chem Eng Sci 1985;40(10):1817–23.
[26] Yang N, Wang W, Ge W, Li J. CFD simulation of concurrent-up gas–solid flow in circulating fluidized beds with structure-dependent drag coefficient. Chem Eng Sci 2003;96(1):71–80.
[27] Schiller L, Naumann A. Uber die grundlengenden berechungen bei schwerkraftaufbereitung. Z Ver Dtsch Ing 1933;77:318–20.
[28] McKeen T, Pugsley T. Simulation and experimental validation of a freely bubbling bed of FCC catalyst. Powder Technol 2003;129(1):139–52.
[29] Oliveira PJ, Issa RI. Numerical aspects of an algorithm for the Eulerian simulation of two-phase flows. Int J Numer Methods Fluids 2003;43(10–11):1177–98.
[30] Weller H. Derivation, modelling and solution of the conditionally averaged two-phase flow equations. Technical Report TR/HGW/02. Nabla Ltd.; 2002.
[31] Passalacqua A, Fox RO. Implementation of an iterative solution procedure for multi-fluid gas–particle flow models on unstructured grids. Powder Technol 2011;213(1):174–87.
[32] LeVeque RJ. Finite volume methods for hyperbolic problems, 31. Cambridge University Press; 2002.
[33] Park I, Cho H, Yoon H, Jeong J. Numerical effects of the semi-conservative form of momentum equations for multi-dimensional two-phase flows. Nucl Eng Des 2009;239(11):2365–71.
[34] Weller HG, Tabor G, Jasak H, Fureby C. A tensorial approach to computational continuum mechanics using object-oriented techniques. Comput Phys 1998;12(6):620–31.
[35] Oliveira PJ, Issa RI. On the numerical treatment of interphase forces in two-phase flow. ASME-PUBLICATIONS-FED 1994;185:131.
[36] Spalding D. Numerical computation of multi-phase fluid flow and heat transfer. Recent Adv Numer Methods Fluids 1980;1:139–67.
[37] Miller TF, Miller DJ. A Fourier analysis of the IPSA/PEA algorithms applied to multiphase flows with mass transfer. Comput Fluids 2003;32(2):197–221.
[38] Karema H, Lo S. Efficiency of interphase coupling algorithms in fluidized bed conditions. Comput Fluids 1999;28(3):323–60.
[39] Syamlal M, Rogers W, O'Brien TJ. MFIX documentation: theory guide. Technical Note DOE/METC-95/1013 and NTIS/DE95000031. National Energy Technology Laboratory, Department of Energy; 1993.
[40] Patankar SV, Spalding DB. A calculation procedure for heat, mass and momentum transfer in three-dimensional parabolic flows. Int J Heat Mass Transf 1972;15(10):1787–806.
[41] Issa RI. Solution of the implicitly discretised fluid flow equations by operator-splitting. J Comput Phys 1986;62(1):40–65.
[42] Deshpande SS, Anumolu L, Trujillo MF. Evaluating the performance of the two-phase flow solver interFoam. Comput Sci Discov 2012;5(1):014016.
[43] Márquez Damián S. An extended mixture model for the simultaneous treatment of short and long scale interfaces [Ph.D. thesis]. Universidad Nacional del Litoral; 2013.
[44] Zalesak ST. Fully multidimensional flux-corrected transport algorithms for fluids. J Comput Phys 1979;31(3):335–62.
[45] Carnahan NF, Starling KE. Equation of state for nonattracting rigid spheres. J Chem Phys 1969;51(2):635–6.
[46] Ferziger JH, Peric M. Computational methods for fluid dynamics. Springer Science & Business Media; 2012.
[47] Jasak H. Error analysis and estimation for the finite volume method with applications to fluid flows [Ph.D. thesis]. Imperial College of Science, Technology and Medicine; 1996.
[48] Liu Y, Hinrichsen O. CFD modeling of bubbling fluidized beds using OpenFOAM®: model validation and comparison of TVD differencing schemes. Comput Chem Eng 2014;69:75–88.
[49] Nigam M. Numerical simulation of buoyant mixture flows. Int J Multiph Flow 2003;29(6):983–1015.
[50] Márquez Damián S, Nigro NM. An extended mixture model for the simultaneous treatment of small-scale and large-scale interfaces. Int J Numer Methods Fluids 2014;75(8):547–74.
[51] Benyahia S, Syamlal M, O'Brien TJ. Evaluation of boundary conditions used to model dilute, turbulent gas/solids flows in a pipe. Powder Technol 2005;156(2):62–72.
[52] Fede P, Simonin O, Ingram A. 3D numerical simulation of a lab-scale pressurized dense fluidized bed focussing on the effect of the particle-particle restitution coefficient and particle–wall boundary conditions. Chem Eng Sci 2016;142:215–35.
[53] Li T. Validation of a 2.5D CFD model for cylindrical gas–solids fluidized beds. Powder Technol 2015;286:817–27.
[54] Cloete S, Zaabout A, Johansen ST, van Sint Annaland M, Gallucci F, Amini S. The generality of the standard 2D TFM approach in predicting bubbling fluidized bed hydrodynamics. Powder Technol 2013;235:735–46.
[55] Hernández-Jiménez F, Sánchez-Delgado S, Gómez-García A, Acosta-Iborra A. Comparison between two-fluid model simulations and particle image analysis & velocimetry (PIV) results for a two-dimensional gas–solid fluidized bed. Chem Eng Sci 2011;66(17):3753–72.
[56] Rider WJ, Kothe DB. Reconstructing volume tracking. J Comput Phys 1998;141(2):112–52.
[57] FluentInc.. FLUENT 6.1 UDF manual. Fluent, Inc.; 2003. p. 14–16.
[58] Spore J, Elson J, Jolly-Woodruff S, Knight T, Lin J, Nelson R, et al. TRAC-M/FORTRAN 90 (version 3.0) – theory manual. Los Alamos National Laboratory; 2000.
[59] Sharp DH. An overview of Rayleigh–Taylor instability. Phys D: Nonlinear Phenom 1984;12(1):3–18.
[60] Kuipers J, Prins W, Van Swaaij W. Theoretical and experimental bubble formation at a single orifice in a two-dimensional gas-fluidized bed. Chem Eng Sci 1991;46(11):2881–94.
[61] Passalacqua A, Marmo L. A critical comparison of frictional stress models applied to the simulation of bubbling fluidized beds. Chem Eng Sci 2009;64(12):2795–806.